Biomaterials 301 (2023) 122237

Contents lists available at ScienceDirect

Biomaterials

journal homepage: www.elsevier.com/locate/biomaterials

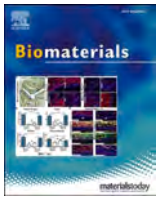

pH/NIR-responsive and self-healing coatings with bacteria killing, osteogenesis, and angiogenesis performances on magnesium alloy

Yanbin Zhao [a,b,1], Peng He [c,1], Junyan Yao [a,b], Mei Li [d], Bin Wang [e], Linyuan Han [a,b], Zhihai Huang [a,b], Chao Guo [a,b], Jing Bai [a,b], Feng Xue [a,b], Yu Cong [f,**], Weihua Cai [g,***], Paul K. Chu [h], Chenglin Chu [a,b,*]

[a] School of Materials Science and Engineering, Southeast University, Nanjing, 211189, China
[b] Jiangsu Key Laboratory for Advanced Metallic Materials, Southeast University, Nanjing, 211189, China
[c] Department of Orthopedics, The Affiliated Jinling Hospital of Nanjing Medical University, Nanjing, 211166, China
[d] Medical Research Center, Department of Orthopedics, Guangdong Provincial People's Hospital, Guangdong Academy of Medical Sciences, Guangzhou, 510080, China
[e] Department of Orthopedics, Jinling Hospital, School of Medicine, Nanjing University, Nanjing, 210093, China
[f] Jinling Hospital Department of Orthopedics, Southeast University, School of Medicine, Nanjing, 210002, China
[g] Department of Orthopedics, The First Affiliated Hospital of Nanjing Medical University, Nanjing, 210029, China
[h] Department of Physics, Department of Materials Science and Engineering, and Department of Biomedical Engineering, City University of Hong Kong, Tat Chee Avenue, Kowloon, Hong Kong, China

ARTICLE INFO

Keywords:
Biodegradable magnesium alloy
Osteogenesis
Angiogenesis
Bacteria killing
Self-healing coating
Controlled release

ABSTRACT

Although biodegradable polymer coatings can impede corrosion of magnesium (Mg)-based orthopedic implants, they are prone to excessive degradation and accidental scratching in practice. Bone implant-related infection and limited osteointegration are other factors that adversely impact clinical application of Mg-based biomedical implants. Herein, a self-healing polymeric coating is constructed on the Mg alloy together with incorporation of a stimuli-responsive drug delivery nanoplatform by a spin-spray layer-by-layer (SSLbL) assembly technique. The nanocontainers are based on simvastatin (SIM)-encapsulated hollow mesoporous silica nanoparticles (S@HMSs) modified with polydopamine (PDA) and polycaprolactone diacrylate (PCL-DA) bilayer. Owing to the dynamic reversible reactions, the hybrid coating shows a fast, stable, and cyclical water-enabled self-healing capacity. The antibacterial assay indicates good bacteria-killing properties under near infrared (NIR) irradiation due to synergistic effects of hyperthermia, reactive oxygens species (ROS), and SIM leaching. *In vitro* results demonstrate that NIR laser irradiation promotes the cytocompatibility, osteogenesis, and angiogenesis. The coating facilitates alkaline phosphatase activity and expedites extracellular matrix mineralization as well as expression of osteogenesis-related genes. This study reveals a useful strategy to develop multifunctional coatings on bioabsorbable Mg alloys for orthopedic implants.

1. Introduction

Musculoskeletal disorders related to age and exercise have increased the social and medical burdens [1,2]. Biodegradable metals (BMs) can break down during tissue regrowth and therefore are suitable orthopedic implant materials [3,4]. Especially, magnesium (Mg) alloys are desirable temporary materials due to excellent mechanical strength and natural biodegradability in physiological environments [5–8]. However, the high corrosion rate can cause premature mechanical failure before complete healing bone tissues [9–11]. Bacterial infections and limited osteointegration are other obstacles hampering clinical adoption of Mg-based orthopedic implants [12–14].

Several approaches have been developed to address these shortcomings, and surface modification and coating treatment are attractive for Mg alloys [15–17]. Layer-by-layer (LbL) assembly is one of the versatile techniques to prepare coatings composed of polymers,

* Corresponding author. School of Materials Science and Engineering, Southeast University, No.2 SEU Road, Nanjing, 211189, China.
** Corresponding author.
*** Corresponding author.
E-mail addresses: congyu122@126.com (Y. Cong), caiwhspine@sina.com (W. Cai), clchu@seu.edu.cn (C. Chu).
[1] These authors contributed equally to this work.

https://doi.org/10.1016/j.biomaterials.2023.122237
Received 9 October 2022; Received in revised form 24 June 2023; Accepted 2 July 2023
Available online 14 July 2023

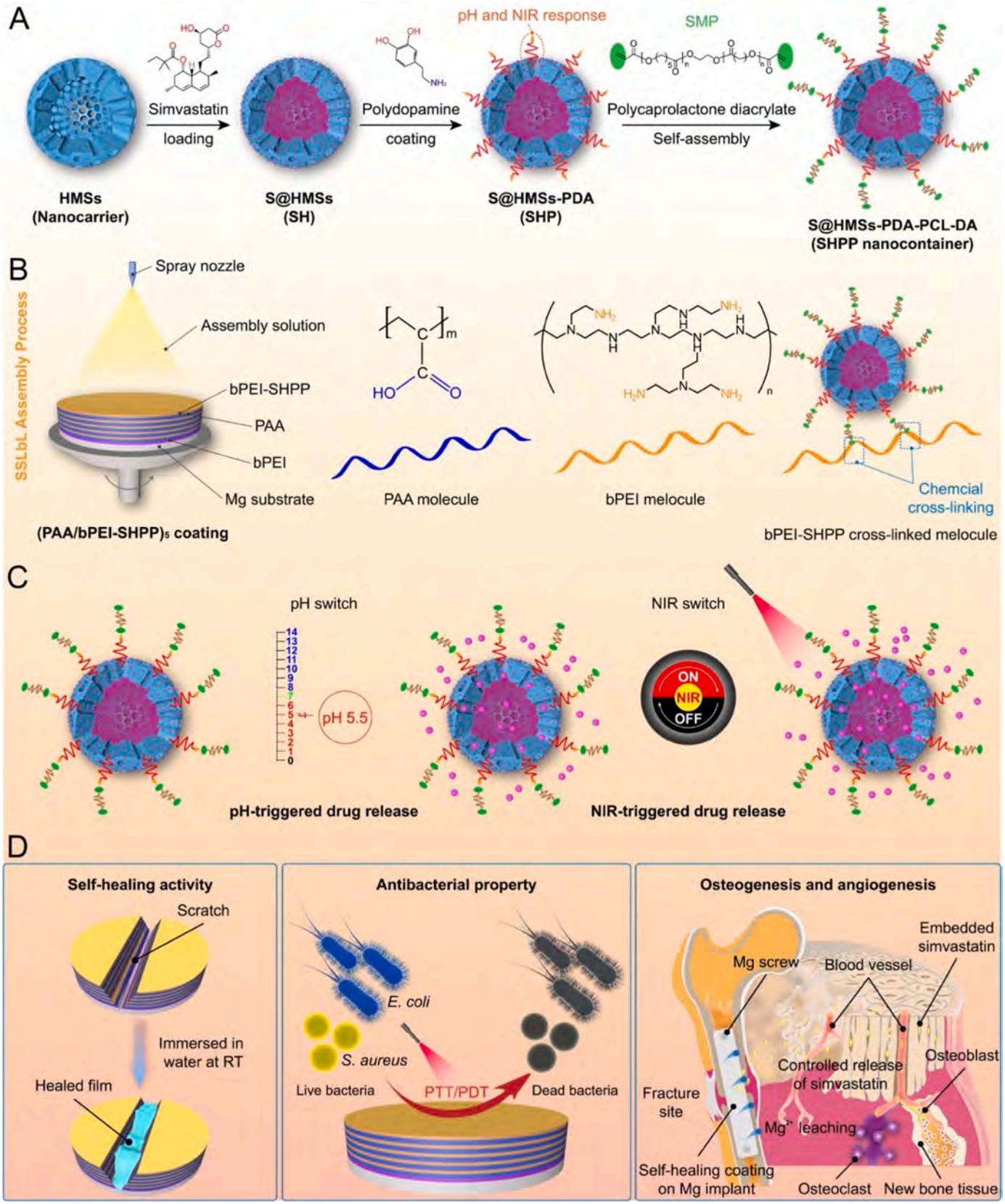

Fig. 1. Schematic illustration of the experimental flow: (A) Fabrication of SHPP nanocontainers, (B) SSLbL assembly, (C) pH- and NIR-triggered drug release assays, and (D) Evaluation of self-healing activity, antibacterial Property, osteogenesis, and angiogenesis.

nanoparticles, proteins, or DNA [18,19]. LbL assembly is performed by alternatively adsorbing oppositely charged materials onto substrate *via* electrostatic interactions, host-guest interaction, as well as hydrogen bonds [20–22]. LbL-assembled polymeric coatings can also offer good corrosion protection to Mg alloys [23–26]. However, the protective surface is temporary and corrosion can be propagated to the substrate through physical defects [27], and therefore LbL-assembled thin films are sopposed to possess the self-healing ability [28,29]. Generally, self-healing behavior involves two strategies. One is the extrinsic healing, scratches are sealed automatically by healable agents such as corrosion inhibitors [30–32], and the other is the intrinsic curing, the damaged surface is repaired by chain rearrangement of the polymer molecules or intramolecular reversible chemical bonds including amide bond, disulfide bond, and others [33–36]. An extrinsic healable film tends to have a heterogeneous distribution, unstable composition, and limited effects, whereas the intrinsic one can cure large scratches of several hundred micrometers in size and undergo multiple damage/healing cycles under appropriate conditions [37–39]. Therefore, this work investigated intrinsic self-healing polyelectrolyte multilayered (PEM) coatings fabricated by a spin-spray LbL (SSLbL) assembly technique. The PEM coatings are constructed by strong coupling of branched poly (ethylenimine)/poly (acrylic acid) (bPEI/PAA) and can self-heal in water due to dynamic reversible reactions of hydrated polymers in multilayered coatings [40,41].

Osteogenesis is another concern for orthopedic implants and infections also pose serious risks and complications after surgery [42–44]. Adhesion of osteoblasts and bacteria on implants materials is a competitive process between osteogenesis and biofilm formation [45]. As the golden standard for bone repair, autografts exhibit positive effects but also suffer from limited bone mass and pain after surgery [46–48]. Allografts as the substitute are also plagued by infection and immune rejection [49,50]. Local drug delivery systems (LDDSs) composed of nanocarriers and bone growth factors constitute a novel strategy in orthopedics but growth factors have poor stability and limited shelf life, whereas osteogenic drugs possess positive effects on LDDSs [51,52]. It is reported that statins tend to trigger the generation of bone morphogenetic protein-2 (BMP-2) in osteoblasts and indicate potential promotion of anabolic effects in skeletons [53,54]. Simvastatin (SIM), a cholesterol-lowering drug that inhibits 3-hydroxy-3-methylglutaryl-coenzyme A (HMG-CoA) reductase, can sustain the differentiation of BMP-induced osteoblasts through restraining the TNF-α-to-MAPK pathway, and thus improve BMP-Smad signaling [55–57]. Simvastatin accelerates the expression of the vascular endothelial growth factor (VEGF) and promotes proliferation and differentiation of vascular endothelial cells, thereby enhancing angiogenesis-coupled osteogenesis [58,59]. Furthermore, simvastatin reduces systemic and vascular inflammation response by inhibiting the leaching of C-Reactive Protein (Ls-CRP) [60–62].

Antibiotic treatment is the main strategy to improve the bacteria-killing effects of bone implants, but due to the abuse of antibiotics, bacterial resistance or even superbugs may emerge [63,64]. As an alternative method, the photothermal/photodynamic therapies (PTT/PDT) can endow specific materials with the high penetration and remote-controlled sterilization ability, as well as hyperthermia and radical oxygen species (ROS) generated by light irradiation can kill bacteria [65,66]. However, photosensitizers-mediated oxygen consumption exacerbates tissue hypoxia and then inhibits the PDT effect [67]. In PTT, effective bacteria killing requires a relatively high temperature, which may cause damage to normal tissues [64,68]. The maximum tolerable temperature of human body is 50–60 °C which may not be sufficient to achieve optimum antibacterial efficiency [69].

Owing to the poor chemical stability and low solubility, simvastatin must be encapsulated in nanocarriers to prolong the drug release. Hollow mesoporous silica nanospheres (HMSs) with a mesoporous outer shell and an interior hollow interior cavity have been used as nanostructured vehicles to load drugs or reagents, which is an easy-to-operate, cost-effective, and controllable method [70–73]. To precisely control the leaching of simvastatin from the nanocontainers, polydopamine (PDA) with abundant amine and catechol bindings is employed in surface modification of HMSs as a pH- and NIR-sensitive polymer "gatekeeper" [74–76]. We have proposed biodegradable poly (ε-caprolactone)diacrylate (PCL-DA) as the switching segments to safeguard the HMSs-based drug loaded nanocarriers from biodegradation [77–79]. As a thermoresponsive shape memory polymer (SMP), PCL-DA molecules become malleable when heated and then expand to fill defects and lock into a new shape [80].

In this work, a novel self-healing coating with the dual pH- and NIR-responsive capacities was constructed on the Mg substrate. Drug-loaded nanocapsules were introduced to the polymer coating by a SSLbL assembly technology. The PAA and bPEI served as the assembly units in the self-assembly process to produce the hybrid coating with multiple functions including bacteria killing, osteogenesis, and angiogenesis (Fig. 1).

Table 1
Chemical composition of WE43 Mg alloy (wt.%).

Mg	Y	Nb	Gd	Zr	Cu	Ni	Fe
Balance	4.05	2.47	1.17	0.52	0.013	0.001	0.001

2. Materials and methods

2.1. Materials

The as-extruded Mg alloy WE43 was purchased from Suzhou Rongqian Rare Metal Product Co., Ltd. And the chemical composition was shown in Table 1. Polyacrylic acid (PAA, *Mw*: 3000 g mol^{-1}, 30%) and polycaprolactone-diol (PCL-diol, *Mn*: ~2000 g mol^{-1}, 99%) were purchased from Shanghai Macklin Biochemical Co., Ltd. And the branched polyethyleneimine (bPEI, *Mw*: 30 k g mol^{-1}, 99%) and tetraethyl orthosilicate (TEOS, *Fw*: 208.33 g mol^{-1}, ≥99%) were acquired from Shandong Xiya Chemical Technology Co., Ltd. Simvastatin (SIM, *Mw*: 418.57 g mol^{-1}, ≥97%), octadecyltrimethoxysilane (C_{18}TMS, *Mw*: 374.67 g mol^{-1}, 90%), dopamine hydrochloride (Dopa·HCl, *Mw*: 189.64 g mol^{-1}, 98%), triethylamine (Et_3N, *Mw*: 101.19 g mol^{-1}, >99.5%), 4-(dimethylamino)pyridine (DMAP, 22.17 g mol^{-1}, 99%), acryloyl chloride (AC, 90.51 g mol^{-1}, 96%), 2,2-dimethoxy-2-phenylacetophenone (DMP, 256.3 g mol^{-1}, 99%), ethyl acetate (88.105 g mol^{-1}, ≥99.5%), and 1-vinyl-2-pyrrolidinone (NVP, 111.14 g mol^{-1}, 99%) were obtained from Shanghai Aladdin Biochemical Technology Co., Ltd. The ammonia solution (35.05 g mol^{-1}, 25–28%), sodium carbonate (105.99 g mol^{-1}, ≥99.8%), potassium carbonate (138.206 g mol^{-1}, ≥98.0%), anhydrous magnesium sulfate (120.37 g mol^{-1}, ≥97.0%) and dichloromethane (DCM, 84.933 g mol^{-1}, ≥99.5%) were bought from Sinopharm Chemical Reagent Co., Ltd. All the reagents were used without purification and ultrapure (UP) water was produced by a Milli-Q water system.

2.2. Synthesis of HMSs

The monodispersed HMSs were synthesized by the combination of the modified Stöber and sol-gel methods. Briefly, 71.4 mL of ethanol, 10 mL of UP water, and 1.57 mL of the ammonia solution were mixed at 30 °C and then 3.5 mL of TEOS was quickly injected and stirred for 2 h. A mixture containing 2.5 mL of TEOS and 1 mL of C_{18}TMS was added to the above solution and mixed for another 1 h to obtain the solid silica core/mesoporous silica shell nanospheres (designated as "sSiO_2@m-SiO_2"), which was dispersed in a 0.3 M of sodium carbonate aqueous solution at 85 °C and stirred for 0.5 h. The products were collected by centrifugation (8000 rpm for 30 min), washed with ethanol and UP water three times, and dried under vacuum overnight. The HMSs were formed by calcination at 813.15 K for 6 h at a heating rate of 1 K min^{-1}.

2.3. Synthesis of PCL-DA

The PCL-DA as a shape memory polymer was synthesized according to an established protocol including acylation reaction and purification of the crude product [77]. In Brief, 0.17 g mL^{-1} of PCL-diol (*Mn*: ~2000 g mol^{-1}) was dissolved in DCM solvent and stirred at 300 rpm for 1 h, and 0.055 mg mL^{-1} of DMAP was added to the solution and mixed for 5 min. Then, 0.033 mM of Et_3N and 0.067 mM of acryloyl chloride were added dropwise to the mixture and the reactor was transferred to an oil bath and incubated overnight. The DCM solvent was removed using a rotary evaporator to obtain the crude PCL-DA. To purify the product, the crude PCL-DA was dissolved in 135 mL of ethyl acetate. Gravity filtration was adopted to remove impurities and ethyl acetate was dislodged by rotation. The as-prepared PCL-DA was dissolved in 140 mL of DCM, and 13.5 mL of 2 M K_2CO_3 was added. The organic layer on the bottom was collected and 5 g of $MgSO_4$ was mixed. Finally, the DCM solvent was removed under vacuum and the obtained PCL-DA was kept away from light.

2.4. Preparation of SHPP nanocontainers

Simvastatin was directly loaded into the synthesized HMSs. Briefly, 500 mg of HMSs were added to 50 mL of the SIM solution (10, 20 and 50 mM in ethanol) and incubated for 1, 2, 4, 8, and 12 h. The SIM-loaded HMSs (S@HMSs, SH) were collected by centrifugation (6000 rpm for 15 min), washed three times, and dried at 37.5 °C overnight. Afterward, the S@HMSs were coated with Dopa·HCl in Tris buffer (10 mM, pH 8.5). Specifically, 500 mg of S@HMSs were added to 100 mL of the dopamine solution with different concentrations (1, 2 and 5 mg mL^{-1}) in the dark for 1, 3 and 6 h, respectively. After the centrifugation-washing-drying cycling, the polydopamine coated S@HMSs (S@HMSs-PDA, SHP) were obtained. The PCL-DA was used in surface modification of SHP. 200 mg of SHP were added to the PCL-DA solution (1 mM in 30 mL of DCM solvent) and mixed for 4 h. The suspension was centrifuged, washed, and dried to obtain the PCL-DA modified S@HMSs-PDA (S@HMSs-PDA-PCL-DA, SHPP) nanocontainers.

2.5. Fabrication of PAA/bPEI-SHPP hybrid coatings

The bPEI-SHPP assembly unit was prepared by chemical cross-linking. Briefly, 1 mg mL^{-1} of SHPP, 10 mg mL^{-1} of bPEI, 4 mg mL^{-1} of EDC, and 1 mg mL^{-1} of NHS were added to water (pH 9.5) and mixed for 2 h in the dark to obtain the bPEI-SHPP materials. Before preparing the coating, WE43 Mg alloy with dimensions of 20 mm × 20 mm × 5 mm was polished up to 3000 grit, rinsed, and dried in warm air. The Mg samples were alkalized with sodium hydroxide for 20 min. In SSLbL assembly process, Mg substrate was spin-coated with 0.5 mL of bPEI solution (10 mg mL^{-1}, pH 9.5) to fabricate a precursor layer and then deposited with 0.3 mL of PAA (10 mg mL^{-1}, pH 7.0) and 0.3 mL of bPEI-SHPP separately by the SSLbL assembly at 3000 rpm for 10 s. By repeating the alternatively depositing process, the $(PAA/bPEI\text{-}SHPP)_n$ hybrid coating designed with different assembly cycles (*n*) was prepared on Mg alloy. At the same time, the $(PAA/bPEI)_n$ coating as a contrast was fabricated by the same assembly process.

2.6. Materials characterization

Transmission electron microscopy (TEM, Talos F200X S/TEM, USA) and scanning electron microscopy (SEM, Nova Nano SEM450, USA) were used to examine the nanostructure and morphology of HMSs, SHP, and SHPP nanoparticles. Small-angle X-ray scattering (SAXS, Anton Paar SAXSpoint, Australia) was carried out to evaluate the phase of specimen. X-ray diffraction (XRD, Bruker D8-Discover, Germany), Fourier transform infrared spectroscopy (FT-IR, Thermo Scientific Nicolet iS10, USA), and X-ray photoelectron spectroscopy (XPS, Thermo Scientific K-Alpha, USA) were performed to determine the chemical and phase compositions of materials. The average size and size distribution of the nanoparticles were analyzed by using a Malvern Zetasizer Nano ZS90 Dynamic Light Scattering (DLS) system. The N_2 adsorption-desorption isotherms were determined on the Quanta chrome Nova 4000e Micrometric apparatus at 77.35 K. The specific surface area was calculated by the BET method, and the pore size and pore volume were calculated by BJH method using the light of the adsorption branch of isotherms. Differential scanning calorimetry (DSC, TA Q2000, USA) was used to confirm the melting temperature of samples and the Zeta potential was determined by the Dispersion DT310 Zeta Potential Analyzer. The adhesion strength of the hybrid coatings was investigated on the WS-2005 scratch system and by a tape peeling-off method according to ASTM D3359-09.

2.7. Corrosion tests

2.7.1. Electrochemical behavior

The electrochemical workstation PARSTAT 3000 manufactured by Princeton Applied Research was employed to evaluate the electrochemical corrosion process in Hank's balanced salt solution (HBSS). A three-electrode system was used in the electrochemical experiments. The potentiodynamic polarization (PDP) curve was monitored from the cathode to anode at a scanning rate of 1 mV s^{-1} in the potential range from −2.5 to −1.0 V SCE^{-1}. The corrosion current density (i_{corr}, μA cm^{-2}) and potential (E_{corr}, V/SCE) were acquired by Tafel extrapolation of the polarization curve. Electrochemical impedance spectroscopy (EIS) was conducted at the open circuit potential (OCP) with an applied AC amplitude 10 mV from 100 kHz to 0.1 Hz. The equivalent circuits (ECs) were obtained by simulating the EIS data. The name of software used for EIS analyses is ZSimpWin.

2.7.2. Mass loss test

In general, mass monitoring is the simplest and most accurate method for corrosion rate calculation, which represents the average measurement over the entire exposure in a corrosive medium. The ratio of HBSS volume to surface area of Mg-based samples was 100 mL cm^{-2}. Specimens were taken out after 1, 3, 7, 14 and 21 days of immersion, and then dipped into a chromate acid solution (200 g L^{-1} of CrO_3 solution saturated with 10 g L^{-1} of $AgNO_3$) to remove the corrosion products, followed with ultrasonic cleaning. The corrosion rate (*CR*, mm y^{-1}) estimated from mass loss was calculated by formula (1) [81,82]:

$$CR = \frac{8.76 \times 10^4 \times \Delta m}{A \times t \times \rho}, \quad (1)$$

where Δm is the mass loss (g), *A* is the exposed surface area (cm^2), *t* is the total immersion time (h), as well as ρ is the alloy density (g cm^{-3}).

2.7.3. Hydrogen evolution test

The hydrogen evolution experiment was carried out as previously reported [83,84]. The burette-funnel apparatus was used to hold the specimen and the hydrogen level in the burette was recorded. The hydrogen evolution rate (v_H, mL cm^{-2} h^{-1}) was calculated by the following formula (2):

$$v_H = \frac{V}{st}, \quad (2)$$

where *V* is the cumulative hydrogen volume (mL), *s* is the exposed surface area (cm^2), and *t* is the immersion time (h).

To estimate the long-term durability of the samples, three specimens were immersed in HBSS at 37.5 °C for 1, 3 and 10 d, respectively, to detect the extent of corrosion and pH variation. SEM equipped with an energy-dispersive X-ray spectrometry (EDS) was used to observe the morphology and detect the composition of the coating surface after immersion. The composition of the corrosion product was determined by FT-IR, XRD, and XPS.

2.8. Self-healing activity

To evaluate self-healing abilities of samples, the cut-through scratch method was used to imitate the damage caused by long usage of the corrosion-resistant materials. The scratched specimens were immersed in PBS at room temperature, and SEM was performed to observe the scratch-then-healing behavior. The healed region of the scratched coatings was analyzed by EDS and XPS, and EIS was utilized to investigate the changes of the impedance modulus in the low frequency region for several damage-healing cycles. The variation of the water contact angles (CAs) on the coatings after the scratch and healing cycles was monitored. Confocal laser scanning microscopy (CLSM, Olympus LEXT OLS5000 3D, Japan) was used to observe the depth of the scratched coatings in real time. All the coating scratches with widths of 25 and 50 μm were made by a scalpel. The self-healing efficiency (η_t, %) at different immersion time was calculated by formula (3):

$$\eta_t\ (\%) = \frac{d_0 - d_t}{d_0} \times 100\%, \tag{3}$$

where d_0 is the initial scratch depth and d_t is the scratch depth at time *t*.

2.9. Simvastatin loading and controlled release assays

The absorbance of simvastatin was monitored by a dual-beam ultraviolet–visible spectrophotometry (UV–vis, Beijing General Analytical TU-1901, China). The drug loading amount was calculated by the subtraction of free SIM in the washing from the initial amount. The drug loading efficiency (*DLE*, %) was calculated according to equation (4):

$$DLE\ (\%) = \frac{W_0 - W}{W_1} \times 100\%, \tag{4}$$

where W_0 and W are the initial weight and free weight of SIM, as well as W_1 is the total mass of S@HMSs.

pH-triggered cumulative release from SHPP nanocontainers loaded with 50 mM of SIM was investigated at different pH (5.5, 7.4). 5 mg of SH, SHP, and SHPP were packed into dialysis bags (cut-off molecular weight, *MW*: 500 Da) with 1 mL of PBS and then transferred to centrifuge tubes containing 9 mL of PBS (pH 5.5, 7.4). To monitor drug leaking, 5 mL of PBS containing SIM was removed and replaced with 5 mL of fresh PBS. The collected solution was analyzed by UV–vis spectrophotometry and the data were recorded at predetermined time intervals. The amount of released SIM was plotted against time according to a premeasured standard curve of SIM. To evaluate the NIR-responsive release behavior, near infrared lasers with different power densities (0.5, 1.0, and 2.0 W cm^{-2}) were used at specific time points to treat the samples immersed in PBS under different pH conditions and cultured at 37 °C. The collection and replacement process of PBS was carried out as aforementioned. The cumulative drug release rate (*DRR*, %) was calculated by equation (5):

$$DDR\ (\%) = \frac{C_t}{C_0} \times 100\%, \tag{5}$$

where C_t and C_0 are the concentrations of the leached and initially loaded SIM at time *t*.

2.10. Antibacterial assay

The antibacterial effects against Gram-positive *S. aureus* and Gram-negative *E. coli* were evaluated using a spread plate-counting method. The bacterial suspensions were incubated at 37 °C overnight using a shaking incubator and diluted to 10^7 CFU mL^{-1} with a 0.9% of NaCl solution. After incubation for 15 h, the bacteria mixture was added to a cuvette and immersed for 4 and 12 h, respectively. 100 μL of the bacteria (10^5 CFU mL^{-1}) were spread on agar plates and incubated at 37 °C for 15 h. The bacteria-containing plates were photographed and the number of new bacteria colonies was counted.

2.11. Cell culture

Mouse bone marrow mesenchymal stem cells (mBMSCs) were used for cell culture. The cells were cultured in Dulbecco's modified Eagle's medium/F12 medium (DMEM, Gibco, USA) supplemented with 10% of fetal bovine serum and 1% of penicillin streptomycin in the standard culture condition (at 37 °C in 5% CO_2/95% air of humid environment). The culture medium was changed every 48 h throughout incubation. Moreover, human umbilical vein endothelial cells (HUVECs) were cultured according to the manufacturer's protocol to passage 5 in the complete Endothelial Cell Growth Medium-2 (EGMTM-2) medium under the standard cell culture conditions (37 °C, 5%/95% CO_2/air, sterile, humidified environment). The cell morphology was observed at each passage by an optical microscope to ensure that the HUVECs were normal and healthy.

2.12. Cell proliferation and viability

Cell proliferation was monitored using a Cell Counting Kit 8 (CCK-8, Dojindo, Kumamoto, Japan). Before incubation, the Mg-based samples were sterilized with ultraviolet irradiation for 4 h on each side. The extract medium was obtained by incubating specimens in the complete DMEM media with a ratio of 1.25 cm^2 mL^{-1} for 3 days. The mBMSCs and HUVECs were separately incubated on 24-well plates and incubated for 1 day. The medium was renewed with 100 μL of the control group of DMEM or different extract media. After incubation for 1, 3, and 5 days, the extra media were rinsed with PBS and cultured in 10% of CCK-8 solution at 37 °C for 4 h. The absorbance of both cells at 450 nm was measured by a spectrophotometer. The live/dead staining assay was used to determine the cell viability towards the extract of various samples.

2.13. Flow cytometry of apoptotic cells

The effects of extracts on mBMSCs and HUVECs were evaluated by a Annexin V-FITC apoptosis detection kit. The cells were seeded on a 24-well plate (2×10^5) and cultured with DMEM for 1 day. After rinsing with PBS three times, the cells in extracts were cultured for 1 day, digested, and centrifuged. They were resuspended in 195 μL of V-FITC Annexin binding solution to which 5 μL of V-FITC was added. After incubating for 10 min, flow cytometry was performed to evaluate the apoptosis level.

2.14. Surface roughness of coatings and cell morphology observation

The average surface roughness (Ra) of Mg-based samples was measured using the atomic force microscope (AFM, Bruker Dimension ICON, Germany). For direct cell adhesion, the mBMSCs cells were seeded on sterilized samples in 24-well TCPS and cultured for 24 h. Before SEM observation, the specimens were rinsed with sterile PBS three times, and then fixed with 2.5% glutaraldehyde for 2 h. The cell-material constructs were direct mounted without spray gold treatment for SEM investigation using the Zeiss Crossbeam350 FIB-SEM at 1.0 kV.

2.15. Macrophage polarization in vitro

In this study, RAW264.7 mouse macrophage was donated from the Medical Research Center of Guangdong Provincial People's Hospital. Macrophages were incubated in the culture medium (DMEM-F12k 1: 1 with 10% PBS and 1% antibiotics) under the humidified atmosphere with 5% CO_2 at 37 °C. The culture medium was refreshed every two days throughout the whole incubation period. The inflammation-related gene expressions of the macrophages, cultured with the extracts of the three different materials for 3 days, were quantified by RT-PCR. The total RNA

Table 2
Primer sequences used for real-time PCR amplification.

Gene name	Forward sequence	Reverse sequence
GAPDH (human)	CAAGAGCACAAGAGGAAGAGG	CTACATGGCAACTGTGAGGAG
GAPDH (mouse)	TTCCAGGAGCGAGACCCCACTA	GGGCGGAGATGATGACCCTTTT
HIF-α	TCTACCAGTTGCAGCCTGAC	GTTCCCTTCCTCCTTGATTT
VEGF	CAGGACATTGCTGTGCTTTG	CTCAGAAGCAGGTGAGAGTAAG
Runx2	GACTGTGGTTACCGTCATGGC	ACTTGGTTTTTCATAACAGCGGA
ALP	TCCGTGGGCATTGTGACTAC	TGGTGGCATCTCGTTATCCG
OCN	GGTAGTGAACAGACTCCGGC	GGCGGTCTTCAAGCCATACT
COL-1	GCTCCTCTTAGGGGCCACT	ATTGGGGACCCTTAGGCCAT
OPN	TTCTGAGGGACTAACTACGACC	GGCTGTAAAGCTTCTTCTCCTCG

was isolated by the TRizol reagent, which was then reversed transcribed into complementary DNA using the First Strand cDNA Synthesis Kit. The mRNA expression of M1-related genes (TNF-α, IL-6, and IL-1β) and M2-realated genes (CD206, Arg, and IL-10) in RAW264.7 cells were performed.

2.16. Osteogenic differentiation

The alkaline phosphatase (ALP) activity assay was used to evaluate osteogenic differentiation of mBMSCs. The cells were seeded on 24-well plates (5×10^3). The Mg-based materials were co-cultured for 24 h with the medium and osteogenic induction solution including ascorbic acid (50 μg mL^{-1}), β-glycerophosphate (10 mM), and examethasone (10 mM), and then the supernatant was got out and cultured with osteoblasts. The supernatant extracted for 24 h was selected for cell co-culture. After incubation for 7 and 14 days respectively in the osteogenic induction medium, the ALP activity of Mg-based samples was analyzed qualitatively by staining the cells with a BCIP/NBT ALP Chromogenic kit. The optical results were also recorded. The intracellular total protein concentration and ALP were detected by a BCA protein assay kit (Pierce, Thermo Fisher Scientific, USA) and ALP assay kit (Beyotime Biotechnology, China). The enzyme activity (U mg^{-1}) was calculated by normalizing ALP to the protein content. The collagen secretion and ECM mineralization assays were measured by a Alizarin Red S Staining Quantification Assay. After incubation for 7 and 14 days in an osteogenic induction medium, the mBMSCs were fixed with 4% paraformaldehyde and stained with 1% Alizarin Red S (pH 4.2) for 10 min at 4 °C. The Mg-based samples were rinsed with PBS and the staining photos of ECM and calcium nodules were observed by a phase-contrast inverted optical microscope (Olympus, Japan). In the quantitative analysis, 10% of cetylpyridinium chloride was added to the bonded dye and the OD values at 620 nm was recorded by a microplate reader.

2.17. Real-time polymerase chain reaction

The mBMSCs (1×10^5) in the second passage were seeded on 6-well plates. After incubation for 7 and 14 days separately with an osteogenic differentiation medium, the total RNA extracted *via* TRIzol reagent (Invitrogen, USA) was applied to synthesize the complementary DNA (cDNA). The osteogenic-related genes (Runx2, ALP, OCN, OPN and COL I) expressions were analyzed quantitatively using a real-time quantitative polymerase chain reaction (qRT-PCR, PerfectStart Green qPCR SuperMix (Trans), China). The primers of the related genes were listed in Table 2.

2.18. Wound healing and angiogenesis assays

A scarification method was applied to measure the migration of HUVECs. The cells were spread on the Mg-based samples (1×10^5) and incubated at 37 °C for 4 h. The culture media were removed and straight lines were made on the surface with a pipet tip. 1 mL of the fresh culture medium was added and cultured for 8 h. The cells were stained with green live cell dye and cell migration was investigated by a fluorescent microscopy. The angiogenic-related genes (VEGF and HIF-α) expressions were analyzed by qRT-PCR.

2.19. In vivo experiments

Eighteen New Zealand white rabbits weighing 1500–2000g were purchased from the Medical Experimental Animal Center of Jiang Su Province. The animals were randomly divided into Mg, PAA/bPEI, PAA/bPEI-SHPP (NIR+) groups. All surgical steps and postoperative treatments were approved by the Guidelines for Care and Use of Laboratory Animals of Nanjing Medical University and the Animal Ethics Committee of Jin Ling Hospital (2022DZGKJDWLS_0024). Before surgery, animals were shaved, and the surgical site was disinfected. After anesthetization, an incision was made around the knee, which exposed the lateral femoral condyle. A 4 mm-diameter hole was made using a drill through the lateral femoral condyles. The cylinder sample (4 mm in diameter, 10 mm in length) was pressed into the hole, and then the wound was disinfected and gently closed. 4 weeks after surgery, all animals were sacrificed by an overdose of pentobarbitone. A micro-CT scanner (mCT80; Scanco Medical AG, Bruttisellen, Switzerland) was used to analyze the femurs with implants. Furthermore, 3D reconstruction was preformed with Scanco Medical software. For cylindrical implant areas, the following data were analyzed by the software: bone volume/tissue volume (BV/TV), bone mineral density (BMD), trabecular thickness (Tb.th) and trabecular separation (Tb.sp).

Subsequently, the femurs with implants were collected and fixed in 4% paraformaldehyde. After gradient dehydration and embedding in polymethylmethacrylate, tissues were cut into sections by a saw microtome (EXAKT Apparatebau, Germany). Then, VG staining was performed on the sections polished to about 50 μm, and the representative pictures were acquired using a microscope (Olympus, Japan). The osseous tissues were decalcified in EDTA decalcifying solution for 4 weeks, and then, the implants were removed gently from the femurs. The decalcified femurs were then dehydrated, embedded, and cut into 5 μm thick slices. Afterward, the obtained sections were dewaxed in xylene and hydrated in gradient ethanol. Through antigen retrieval and blocking, the sections were incubated with primary antibodies (VEGF, OCN; Servicebio, China) and the goat anti-rabbit IgG secondary antibody (InvivoGen, USA). Finally, the positive protein expression was detected by 3,3′-diaminobenzidine solution (Dako, Denmark) and the hematoxylin counterstaining process and examined using a microscope.

2.20. Statistical analysis

The data were expressed as mean ± standard deviation (SD). Differences among groups were analyzed by the two-way analysis of variance followed by the SNK test using SPSS20.0 software. The statistical significance was defined as $^*p < 0.05$, $^{**}p < 0.01$, $^{***}p < 0.001$.

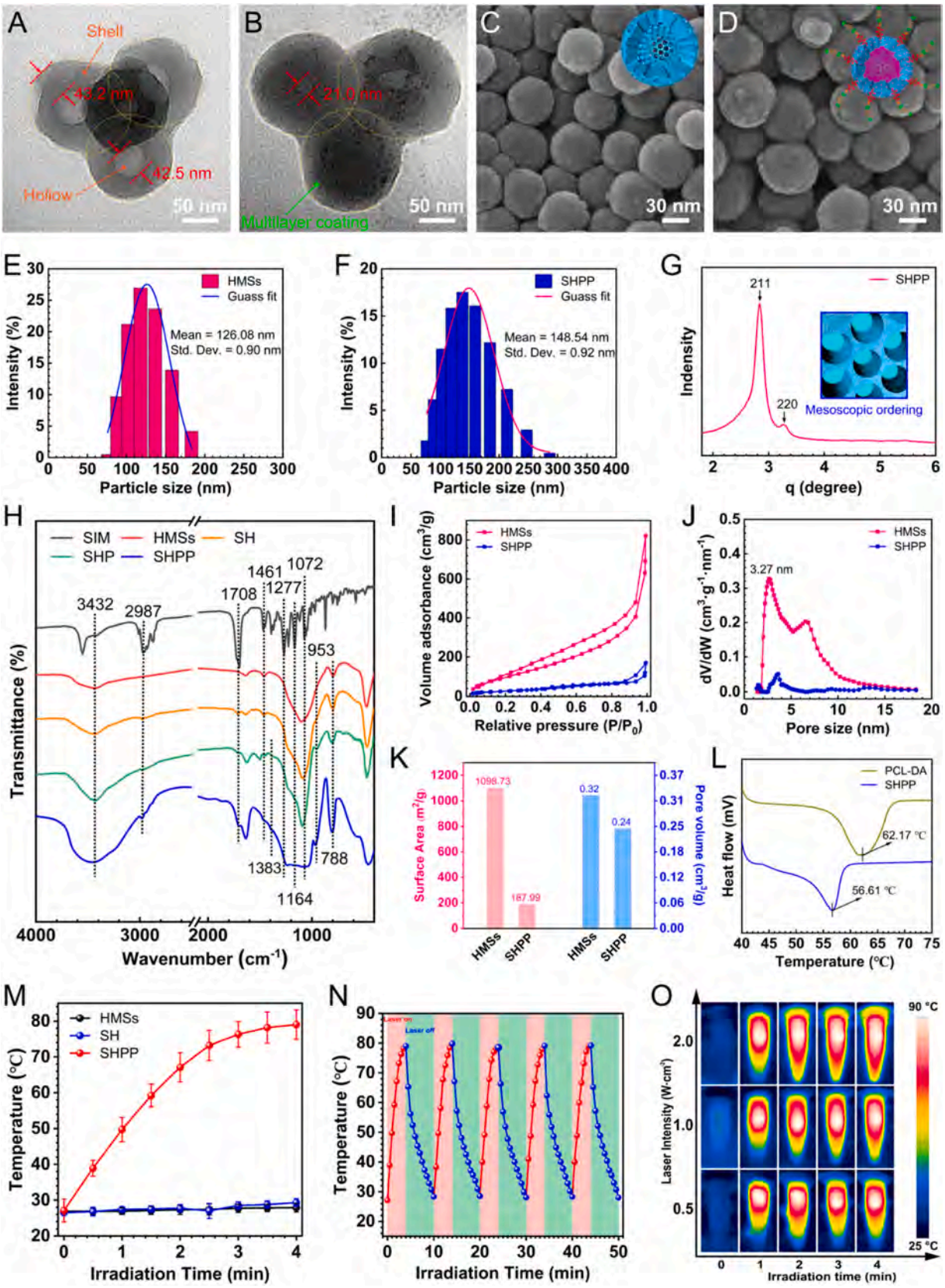

Fig. 2. Characterization of the nanoparticles: TEM images of (A) HMSs and (B) SHPP. SEM morphologies of (C) HMSs and (D) SHPP. DLS analysis of (E) HMSs and (F) SHPP. (G) SAXS patterns of SHPP. (H) FT-IR spectra of materials. (I) N_2 adsorption-desorption isotherms. (J) Pore size distributions calculated by the DFT method. (K) Surface area and pore volume. (L) DSC curves of PCL-DA and SHPP. (M) Photothermal plots of HMSs, SH and SHPP upon laser light irradiation (808 nm, 2.0 W cm^{-2}) for 4 min. (N) Cyclic irradiation profile of SHPP under laser irradiation (808 nm, 2.0 W cm^{-2}) for five on/off cycles. (O) Infrared thermography of SHPP preincubated for different time upon 808 nm laser irradiation with different power densities (0.5, 1.0, and 2.0 W cm^{-2}).

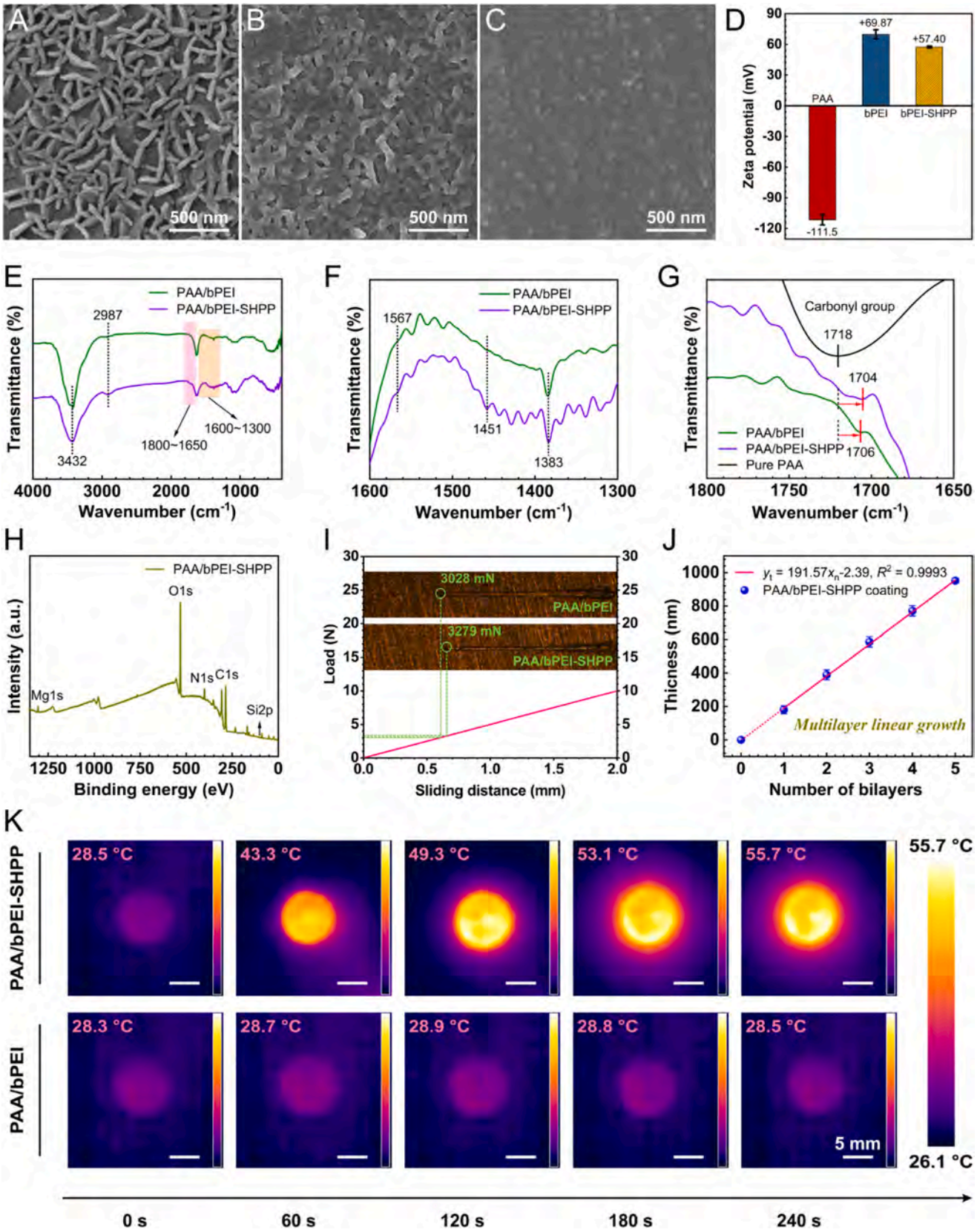

Fig. 3. Characterization of the coatings: SEM morphologies of (A) Bare Mg substrate, (B) $(PAA/bPEI)_5$ coating, and (C) $(PAA/bPEI\text{-}SHPP)_5$ coating. (D) Zeta potentials of PAA, bPEI and bPEI-SHPP. (E–G) FT-IR spectra of the PAA/bPEI film, PAA/bPEI-SHPP coating, and pure PAA. (H) XPS survey spectrum. (I) Scratch tests of the $(PAA/bPEI)_5$ multilayer and $(PAA/bPEI\text{-}SHPP)_5$ coating. (J) Thickness of the PAA/bPEI-SHPP coating with increasing number of bilayers. (K) Infrared thermography of the PAA/bPEI-SHPP and PAA/bPEI coatings.

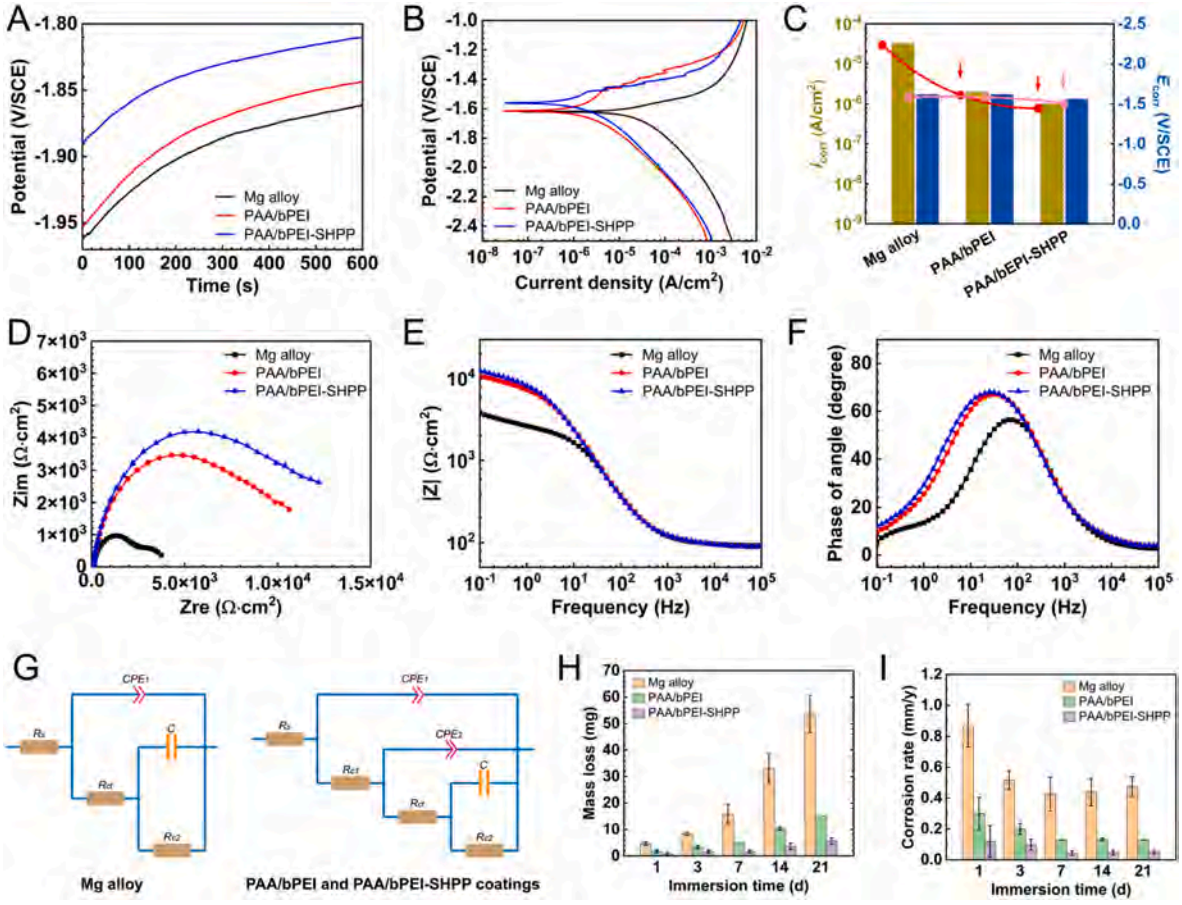

Fig. 4. Electrochemical behavior and mass loss: (A) OCP curves. (B) Polarization curves. (C) I_{corr} and E_{corr}. (D) Nyquist plots. (E) Bode plots. (F) Bode plots of phase angle vs. frequency. (G) ECs of the Mg substrate (left), PAA/bPEI and PAA/bPEI-SHPP coatings (right). (H) Weight loss and (I) corrosion rate of samples during 21 days of immersion in HBSS.

3. Results and discussion

3.1. Nanoparticle characterization

The HMSs nanocarriers are synthesized in a weak alkaline alcohol-water solvent by combining the modified Stöber and sol-gel methods. Considering the permeability of mesoporous shells and the compatibility between the monodispersed HMSs and PDA/PCL-DA bilayer, both the particle size and shell thickness are tailored precisely. In Fig. 2A, the TEM image of HMSs displays a hierarchical hollow mesoporous structure with a hollow cavity (42.5 nm in diameter) and mesoporous shell (43.2 nm of thickness). A crude PDA/PCL-DA layer is coated on the shell surface of HMSs and the cavity becomes smaller after SIM encapsulating (Fig. 2B). Both the HMSs and SHPP nanoparticles (Fig. 2C and D) are monodisperse spheres and the diameter of SHPP is larger than that of HMSs. The DLS test discloses that the average diameters of bare HMSs (Fig. 2E) and SHPP (Fig. 2F) are 126.08 and 148.54 nm, respectively, suggesting that the thickness of PDA/PCL-DA layer on HMSs is about 22.46 nm. The SAXS pattern (Fig. 2G) of SHPP shows two diffraction peaks from the (211) and (220) planes, indicating a mesoscopic ordering in the shell. In Fig. 2H, the pure HMSs constitute the control group showing Si–O–Si vibration and surface silanol bond at 953 and 788 cm^{-1}, separately. As for S@HMSs, the ester C═O stretch is detected at 1708 cm^{-1}. The lactone and ester C–O–C peaks at 1277 and 1164 cm^{-1} and secondary alcohol C–O stretching mode at 1072 cm^{-1} confirm the successful encapsulation of SIM in HMSs [85,86]. After coating PDA on S@HMSs, two new peaks emerge at 1383 and 1451 cm^{-1} representing C–N vibration and N–H stretching, respectively. The band at 1708 cm^{-1} from SHPP represents the stretching of carbonyl in the PCL-DA molecules. The N_2 adsorption-desorption isotherms (Fig. 2I) of HMSs and SHPP show the same type IV curves with hysteresis loops, suggesting that mesopores exist on the shell surface of HMSs-based nanoparticles. Fig. 2J shows that the pore size distributions (PSDs) of both nanoparticles are narrow and that of HMSs (3.27 nm) becomes smaller after PDA and PCL-DA coating. The BET surface area and pore volume of the bare HMSs (1098.73 $m^2 g^{-1}$, 0.32 $cm^3 g^{-1}$) diminish to 187.99 $m^2 g^{-1}$ and 0.24 $cm^3 g^{-1}$ in Fig. 2K. Hence, the HMSs as drug nanocarriers have a high loading capacity due to the hollow core/mesoporous shell architecture.

3.2. Photothermal properties of nanocontainers

DSC analysis (Fig. 2L) reveals the effects of PCL-DA on the thermophysical activity of the nanocapsules. The SHPP nanocontainers exhibit an endothermic peak around 56.61 °C, which is lower than the melting point of PCL-DA (62.17 °C) due to the decreasing crystalline nature of the hybrid materials. Fig. 2M shows that upon 808 nm NIR irradiation (2.0 W cm^{-2}) for 4 h, the temperature of SHPP increases from 27.1 to 79.0 °C. In contrast, the temperature of HMSs and SH remains almost constant after irradiation. The temperature cycling profiles of SHPP infer the photothermal stability of PDA, which are independent of other materials in SHPP (Fig. 2N). The corresponding infrared thermography of SHPP irradiated for 4 h with different power densities are presented in Fig. 2O. The surface temperature of SHPP at the same power density increases rapidly with the extension of irradiation time. After 4 min of irradiation, the temperature of SHPP irradiated with power of 2.0, 1.0 and 0.5 W cm^{-2} reaches 79.0, 52.3 and 43.1 °C, respectively. Therefore, the SHPP nanocontainers have efficient photothermal conversion

Table 3
Fitted electrochemical parameters obtained by EIS simulation.

Samples	R_s ($\Omega \cdot cm^2$)	Q_1 (Ω^{-1} s^n cm^{-2})	n_1	R_{c1} (Ω cm^2)	Q_2 (Ω^{-1} s^n cm^{-2})	n_2	R_{ct} (Ω cm^2)	C (F cm^2)	R_{c2} (Ω cm^2)
Mg alloy	93.73	1.26×10^{-5}	0.80	–	–	–	998	4.55×10^{-4}	2554
PAA/bPEI	88.71	9.48×10^{-7}	0.85	3.20	9.52×10^{-6}	0.88	3008	1.30×10^{-4}	8345
PAA/bPEI-SHPP	89.33	1.07×10^{-6}	0.85	3.62	1.01×10^{-5}	0.82	4245	2.45×10^{-4}	10,000

capacity and superior photostability.

3.3. Coating characterization

The PAA/bPEI-SHPP coating is fabricated on Mg substrate by a SSLbL assembly method. The micro-nano surface structure of WE43 Mg alloy (Fig. 3A) shows a random network due to natural oxidation in air. After the deposition of PAA/bPEI coating, the surface becomes relatively flat (Fig. 3B). In Fig. 3C, the PAA/bPEI-SHPP hybrid coating has a defect-free and smooth surface, indicating that the addition of SHPP improves the physical barrier quality of the SSLbL assembled polymer surface on Mg substrate. The zeta potentials are measured and displayed

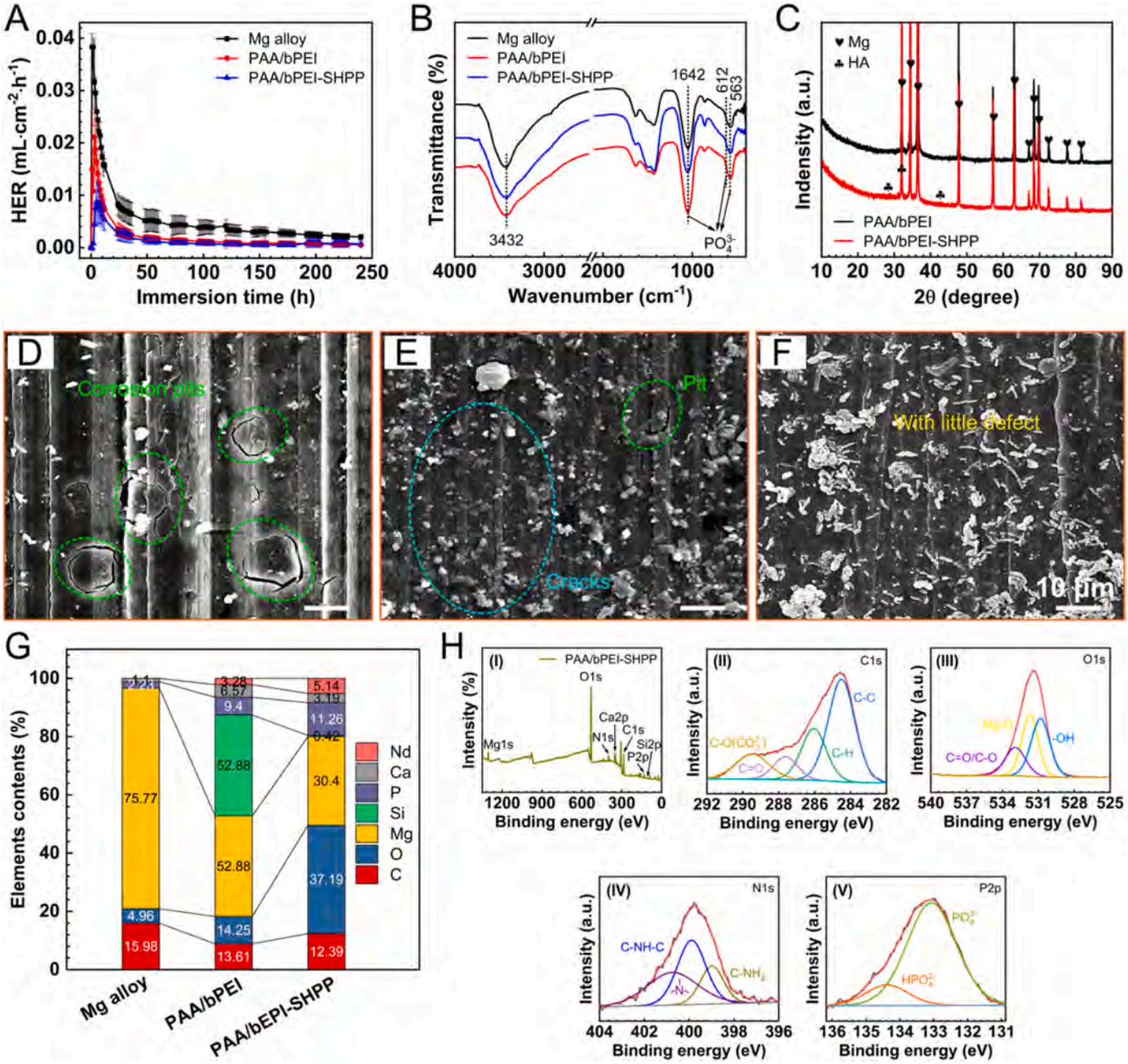

Fig. 5. Immersion measurements during 240 h in HBSS: (A) Hydrogen evolution, (B) FT-IR spectra, (C) XRD patterns of Mg substrate, PAA/bPEI coating, and PAA/bPEI-SHPP coating. SEM morphologies of (D) Mg substrate, (E) PAA/bPEI coating, and (F) PAA/bPEI-SHPP coating. (G) Elements composition of Mg substrate, PAA/bPEI coating, and PAA/bPEI-SHPP coating. (H) XPS spectra of PAA/bPEI-SHPP coating.

in Fig. 3D. The potential of PAA is negative (−111.5 mV) but those of bPEI (+69.87 mV) and bPEI-SHPP (+57.40 mV) are positive. The oppositely charged polyelectrolytes generate electrostatic attraction between each other during the self-healing process. Fig. 3E shows a peak at 2967 cm^{-1} stemming from the stretching of –CH group. The absorption bands at 1,567, 1,454, and 1383 cm^{-1} arise from bending of N–H in primary and secondary amines, respectively (Fig. 3F). To evaluate the interactions between PAA and bPEI-SHPP, FT-IR is conducted on pure PAA as the control group. The absorption peak at 1718 cm^{-1} is attributed to stretching of carbonyl in pure PAA (Fig. 3G). The peaks of –C═O in the PAA/bPEI and PAA/bPEI-SHPP coatings appear at 1704 and 1706 cm^{-1}, respectively, which exhibit red-shifts by 14 and 12 cm^{-1} compared to pure PAA. Hence, hydrogen and amide bonds are formed between PAA and bPEI-SHPP during SSLbL assembly process. The elemental composition and chemical states of PAA/bPEI-SHPP coating are investigated by XPS. Fig. 3H discloses that the hybrid coating contains Mg, O, N, C, and Si. The adhesion strength of PAA/bPEI and PAA/bPEI-SHPP coatings is evaluated by scratch tests and Fig. 3I shows the relationship between critical load (L) and sliding distance. The L values of PAA/bPEI and PAA/bPEI-SHPP films are 3279 and 3028 mN, respectively, demonstrating that incorporating SHPP nanocontainers into the hybrid coating hardly affects the adhesion strength of the PAA/bPEI samples. The thickness of $(PAA/bPEI\text{-}SHPP)_n$ coating increases almost linearly with a slope of 191.57 nm per bilayer and reaches 951.76 ± 15.56 nm after five deposition cycles ($n = 5$). Under 2.0 W cm^{-2} of NIR laser illumination, the temperature of PAA/bPEI-SHPP coating increases rapidly reaching a turning point at about 49.3 °C within 2 min and then stabilizes at 55.7 °C for the remaining 2 min. The temperature of SHPP-incorporated coating is lower than that of the raw SHPP nanoparticles under the same irradiation conditions due to the different densities of SHPP nanoparticles. By comparison, the photothermal properties of PAA/bPEI sample are unstable.

3.4. Corrosion tests

The corrosion properties of samples in HBSS are evaluated by electrochemical test. In OCP curves (Fig. 4A), the potentials (E) exhibit a decreasing trend: $E_{PAA/bPEI\text{-}SHPP} > E_{PAA/bPEI} > E_{Mg\ alloy}$, indicating that the PAA/bPEI-SHPP coating reduces the susceptibility of Mg in HBSS. In PDP plots (Fig. 4B), the values of i_{corr} and E_{corr} are calculated by extrapolation and listed in Fig. 4C. The i_{corr} of the $(PAA/bPEI\text{-}SHPP)_5$ coating (9.87×10^{-7} A cm^{-2}) is smaller than those of WE43 alloy (3.18×10^{-5} A cm^{-2}) and $(PAA/bPEI)_5$ coating (1.95×10^{-6} A cm^{-2}), which demonstrates an excellent corrosion protection for Mg alloy. The E_{corr} of the SHPP-incorporated coating increases by 60 mV SCE^{-1} in the positive potential compared with the bare Mg and the PAA/bPEI coating. From the viewpoint of thermodynamics, the corrosion initiation tendency is upward. In addition, both PAA/bPEI and PAA/bPEI-SHPP coatings show the same breakdown potentials, implying that dissolution is inhibited due to self-healing activity.

In Nyquist plots (Fig. 4D), the capacitive loop diameter in the PAA/bPEI-SHPP coating is larger than those of bare Mg and PAA/bPEI coating, which reflectes a good corrosion resistance. From Bode plots (Fig. 4E), the nanocapsules-containing coating shows a higher low-frequency platform than the other samples, consistent with Nyquist plots. After coating PAA and bPEI-SHPP, the phase angle (Fig. 4F) becomes wider and loftier. Hence, the surface of the PAA/bPEI-SHPP coating is dense and uniform, consistant with SEM. EIS suggests that incorporation of SHPP nanocontainers improves the anti-corrosion capability of PAA/bPEI coating and bare Mg.

To further explore the corrosion mechanism of samples in HBSS, two equivalent circuits (ECs) are adopted to fit the EIS data in Fig. 4G and the corresponding parameters are listed in Table 3. The bare Mg substrate fits the EC in Fig. 4G (left) showing two time constants for R_s ($Q_1(R_f(CR_{ct}))$), where R_s, R_f, and R_{ct} are the solution resistance of specimen-to-electrode, the resistance of corrosion products film, and the resistance of electron transfer across the surface, as well as Q_1 and C are the double layer capacitance and constant phase element (CPE, $Y_{CPE}(\omega) = 1/Z_{CPE} = Q_a\ (j\omega)^n$). Both the $(PAA/bPEI)_5$ and $(PAA/bPEI\text{-}SHPP)_5$ coatings show the same ECs in Fig. 4G (right). The electric double layer contains CPE and R_{ct} in series for the high frequency circuit. Degradation of the PAA/bPEI-SHPP coating is reflected by the intermediate frequency loop with R_{c2} and Q_2, and the low frequency loop (R_{c1} and Q_1) presents the corrosion resistance of corrosion product. The additive time constant of the $(PAA/bPEI\text{-}SHPP)_5$ coating means a better corrosion protection. The mass loss tests of specimens after 1, 3, 7, 14 and 21 days of immersion in corrosive medium are also executed. The mass loss (Fig. 4H) of all bare and coated Mg increases with time. In the three groups, the degradation rates (Fig. 4I) fluctuate throughout the whole immersion process. The average corrosion rate at 21 days shows a decreasing sequence: Mg substrate (0.474 ± 0.064 mm y^{-1}) > PAA/bPEI coating (0.128 ± 0.001 mm y^{-1}) > PAA/bPEI-SHPP coating (0.048 ± 0.011 mm y^{-1}). It indicates that the PAA/bPEI-SHPP coating can reduce the corrosion rate of bare Mg up to ten times.

Immersion experiments are performed to determine the long-term corrosion resistance in Fig. 5. The hydrogen evolution tests are carried out during 240 h of immersion in HBSS in Fig. 5A. The HER curves of the three specimens exhibit the same two stages. In the initial 48 h, hydrogen emission from the three samples decreases rapidly due to the outside-to-inside corrosion of Mg substrate. Thereafter, the corrosion rate slows until reaching a steady state. The average hydrogen evolution rates exhibit the following order: PAA/bPEI-SHPP coating (0.014 ± 0.001 mL cm^{-2} d^{-1}) < PAA/bPEI coating (0.017 ± 0.003 mL cm^{-2} d^{-1}) < Mg substrate (0.049 ± 0.009 mL cm^{-2} d^{-1}). The results confirm that a defect-free SHPP-incorporated coating has long-term corrosion resistance in corrosive media.

In order to determine the composition of corrosion products, FT-IR and XRD are conducted after 240 h of immersion in HBSS. In Fig. 5B, the band at 1042 cm^{-1} represents the stretching of phosphate and those at 612 and 563 cm^{-1} are the bending modes of PO_4^{3-}. The peak of hydroxyl group is appeared at 3432 cm^{-1}. The results show that the PAA/bPEI-SHPP coating promotes the formation of phosphate during corrosion process. In Fig. 5C, the appearance of hydroxyapatite (HAp) confirms that the PAA/bPEI-SHPP coating induces crystallization of HAp in HBSS.

The morphology of samples immersed in HBSS is observed by SEM. There are corrosion pits and large defects on the corroded Mg alloys (Fig. 5D) and the PAA/bPEI coating (Fig. 5E) shows some cracks rather than a few pits and corrosion products. However, micro defects and products appear from the surface of the PAA/bPEI-SHPP coating (Fig. 5F). Fig. 5G shows that both the coated and bare Mg alloys contain Mg, C, O, Ca, and P, consistent with FT-IR and XRD. Particularly, the PAA/bPEI-SHPP coating exhibits a higher content of P element than bare Mg after 240 h of immersion. Besides, the calculated Ca/P ratios of the PAA/bPEI-SHPP coating and the PAA/bPEI coating are 0.28 and 0.70, respectively, both lower than 1.67. It indicates that a calcium-deficient (Ca-def) HAp coating is formed on the substrate surface during immersion [87,88]. The reasonable explanation is that due to the high ionization tendency of magnesium, Mg alloy will be corroded by water, and the released Mg^{2+} ions can replace the Ca^{2+} ions in the HAp architecture [89,90].

The chemical states of corrosion products on the PAA/bPEI-SHPP coating are evaluated by XPS and the Mg 1s, O 1s, N 1s, Ca 2p, C 1s, P 2p and Si 2p spectra are depicted in Fig. 5H. The C 1s spectrum exhibits peaks at 289.48, 287.58, 286.08, and 284.48 eV, representing C–O (CO_3^{2-}), C═O, C–H, and C–C groups, respectively. The O 1s spectrum of hybrid coating shows C═O/C–O (532.48 eV), MgO (531.88 eV) and –OH (530.98 eV) groups. The detected C–NH–C (399.88 eV) and tertiary amine (400.68 eV) confirm the bPEI-assembled coating, and the C–NH_2 peak (398.98 eV) of PDA indicates a compact and defect-free hybrid coating after the immersion in corrosive medium. The P element is observed from the coating due to the formation of the corrosion-induced

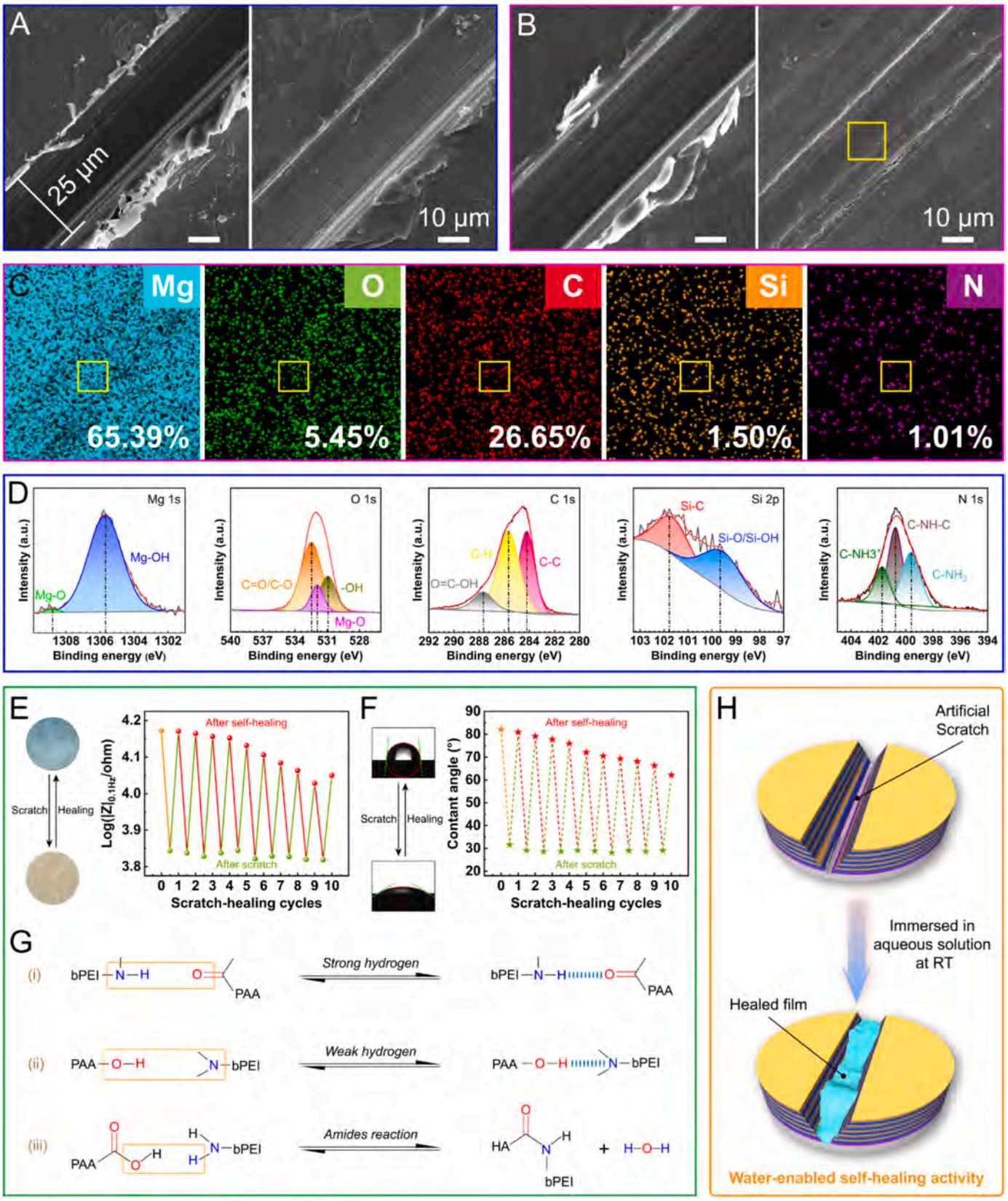

Fig. 6. Self-healing activity and mechanism: SEM morphology: (A) Scratched PAA/bPEI coating before (left) and after (right) 5-h immersion in the aqueous solution at RT. (B) Scratched PAA/bPEI-SHPP hybrid coating before (left) and after (right) 5-h immersion in water at RT. (C) EDS maps of the healed PAA/bPEI-SHPP coating showing Mg, O, C, Si, and N. (D) XPS spectra acquired from the healed region of the PAA/bPEI-SHPP coating. (E) Changes of the impedance modulus of the PAA/bPEI-SHPP coating in the low frequency region for the damage-healing cycles. (F) Variations of the water contact angles on the PAA/bPEI-SHPP coating after repeated artificial scratching and self-healing. (G) Dynamic reversible reaction between the PAA and bPEI molecules driving self-healing. (H) Water-enabled self-healing mechanism of the PAA/bPEI-SHPP coating.

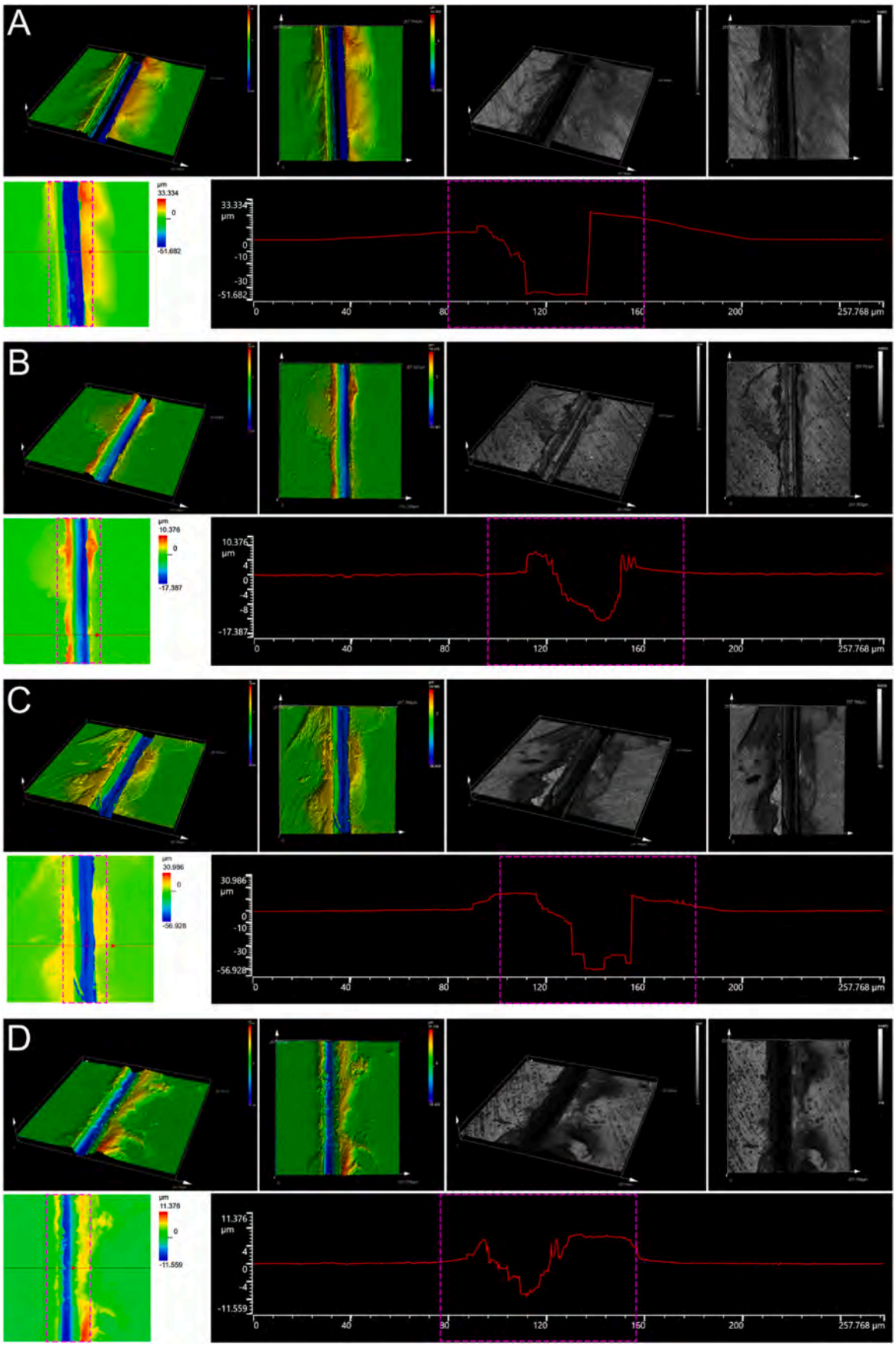

Fig. 7. CLSM assay: CLSM images and depth plots of scratches on (A) PAA/bPEI and (C) PAA/bPEI-SHPP coatings as well as healed (B) PAA/bPEI and (D) PAA/bPEI-SHPP coatings.

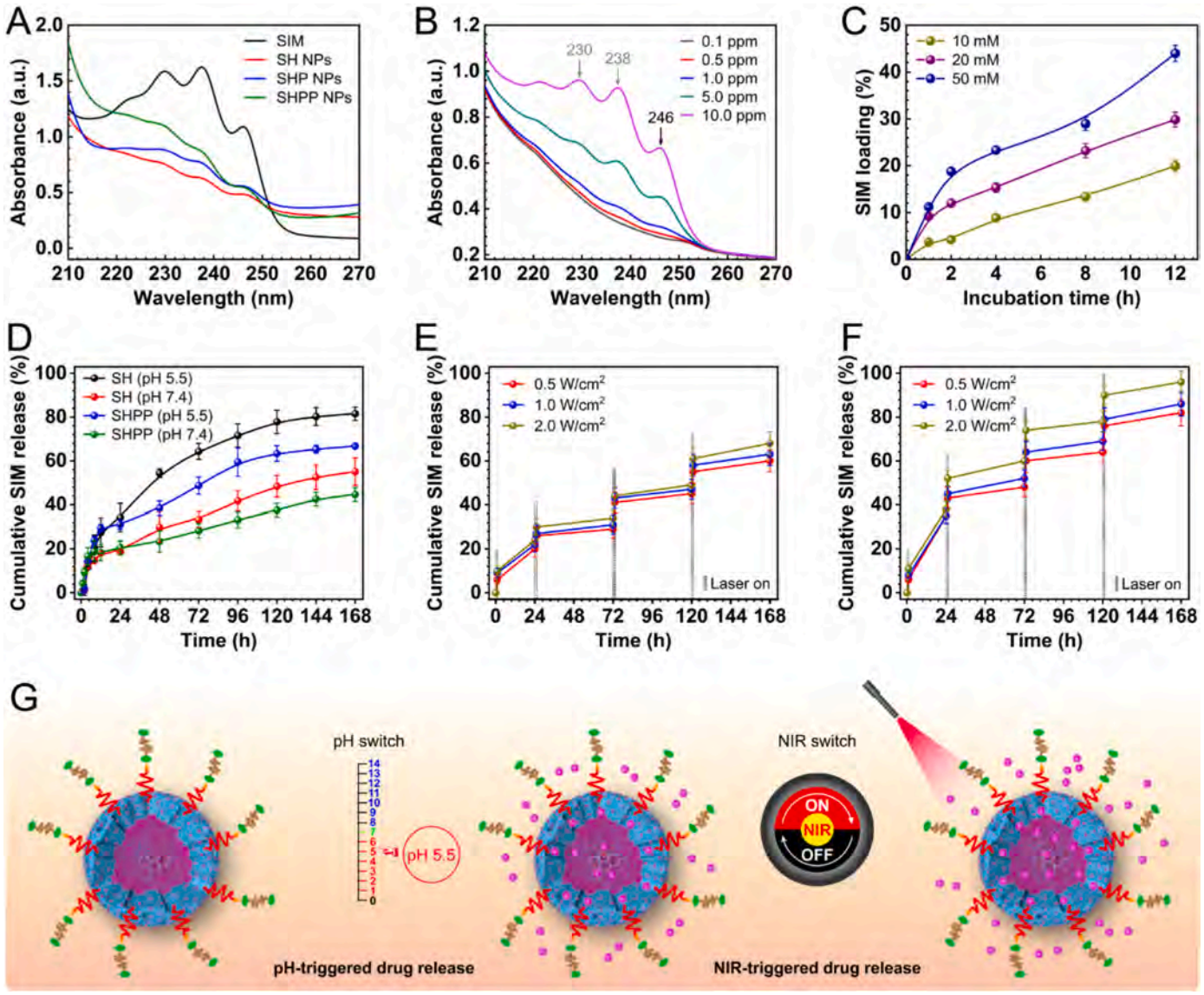

Fig. 8. Drug loading, release profiles, and mechanism: (A) UV–vis spectra. (B) UV–vis plots of the SHPP dispersion with different concentrations. (C) Cumulative loading profiles versus incubation time and concentration of SIM into HMSs. (D) Release profiles of SIM from the SH and SHPP dispersions at pH of 5.5 and 7.4. (E) SIM release profile from SHPP under 808 nm NIR irradiation (0.5, 1.0, and 2.0 W cm^{-2}) in PBS at pH of 7.4. (F) SIM-release profile of SHPP upon 808 nm NIR irradiation (0.5, 1.0 and 2.0 W cm^{-2}) in PBS at pH 5.5. (G) Schematic illustration of pH- and NIR-triggered drug release from the SHPP nanocontainers.

CaP layer. Hence, the hybrid coating has significant effects on the corrosion resistance of Mg alloy.

3.5. Self-healing activity

The self-assembled coating is scratched and the exposed region after soaking in the aqueous solution for 5 h is observed by SEM. In Fig. 6A and B, the initial scratch widths on both the PAA/bPEI and PAA/bPEI-SHPP coatings are about 25 μm for ease of comparison. The scratches on the PAA/bPEI coating can be cured to some extent of immersion for 5 h (Fig. 6A (right)), whereas the PAA/bPEI-SHPP coating is completely healed in Fig. 6B (right). It can be inferred that the PAA and bPEI form a barrier coating with self-healing capability and the SHPP nanocontainers also boost the recovering efficiency. To evaluate the self-healing effects, the exposed area on the scratched-and-healed PAA/bPEI-SHPP coating is analyzed by EDS. Fig. 6C shows a strong Mg signal and the O, C, and N peaks stem from the polymer. Si in the HMSs-based materials migrates or moves to the scratched region after immersion. XPS is also used to determine the chemical composition of the water-enabled self-healing region of PAA/bPEI-SHPP coating. In Fig. 6D, the Mg 1s spectrum exhibits Mg–O (1308.88 eV) and Mg–OH (1305.68 eV). The O 1s spectrum of the hybrid coating dispalys C═O/C–O (532.48 eV), Mg–O (531.88 eV), and –OH (530.98 eV), the C 1s spectrum manifests O═C–OH (287.68 eV), C–H (285.68 eV), and C–C (284.18 eV), the Si 2p spectrum reveals Si–C (101.78 eV) and Si–O/Si–OH (99.88 eV), and the N 1s spectrum exhibits C–NH_3^+ (eV), C–NH–C (eV), and C–NH_2 (eV). These findings confirm that the PAA-bPEI-SHPP framework is reconstructed in the scratched area due to self-healing activity.

The cyclic water-enabled self-healing properties of PAA/bPEI-SHPP coating are characterized by varying the impedance modulus at low frequencies and water contact angle plots. Artificial scratches are created by a scalpel and the damage which penetrate to the Mg substrate and coating is exposed in Fig. 6B (right). The width of the scratch is about 25 μm. Fig. 6E shows the low frequency modulus impedance ($|Z|_{0.1Hz}$) changes of the hybrid coating immersed in 0.01 M sodium chloride upon repeated damage-and-heal cycles. When the coating is scratched, the modulus impedance at 0.1 Hz reduces by one order of

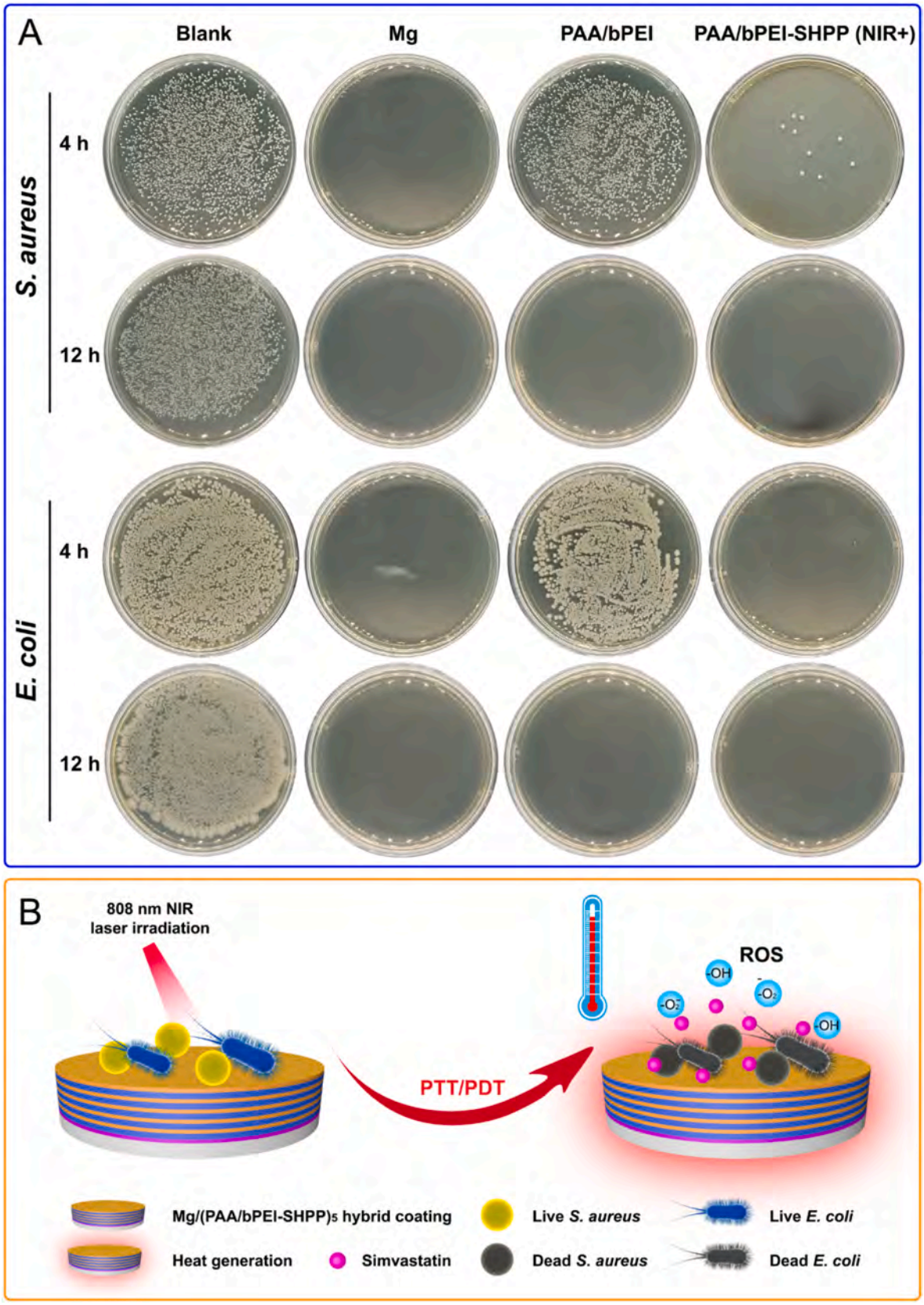

Fig. 9. Antibacterial assay and mechanism: (A) Spread plates of bacterial colonies of *S. aureus* and *E. coli* cultured in extracts for 4 and 12 h together with the blank, bare Mg alloy, PAA/bPEI coating, and NIR-irradiated PAA/bPEI-SHPP coating. (B) Antibacterial mechanism.

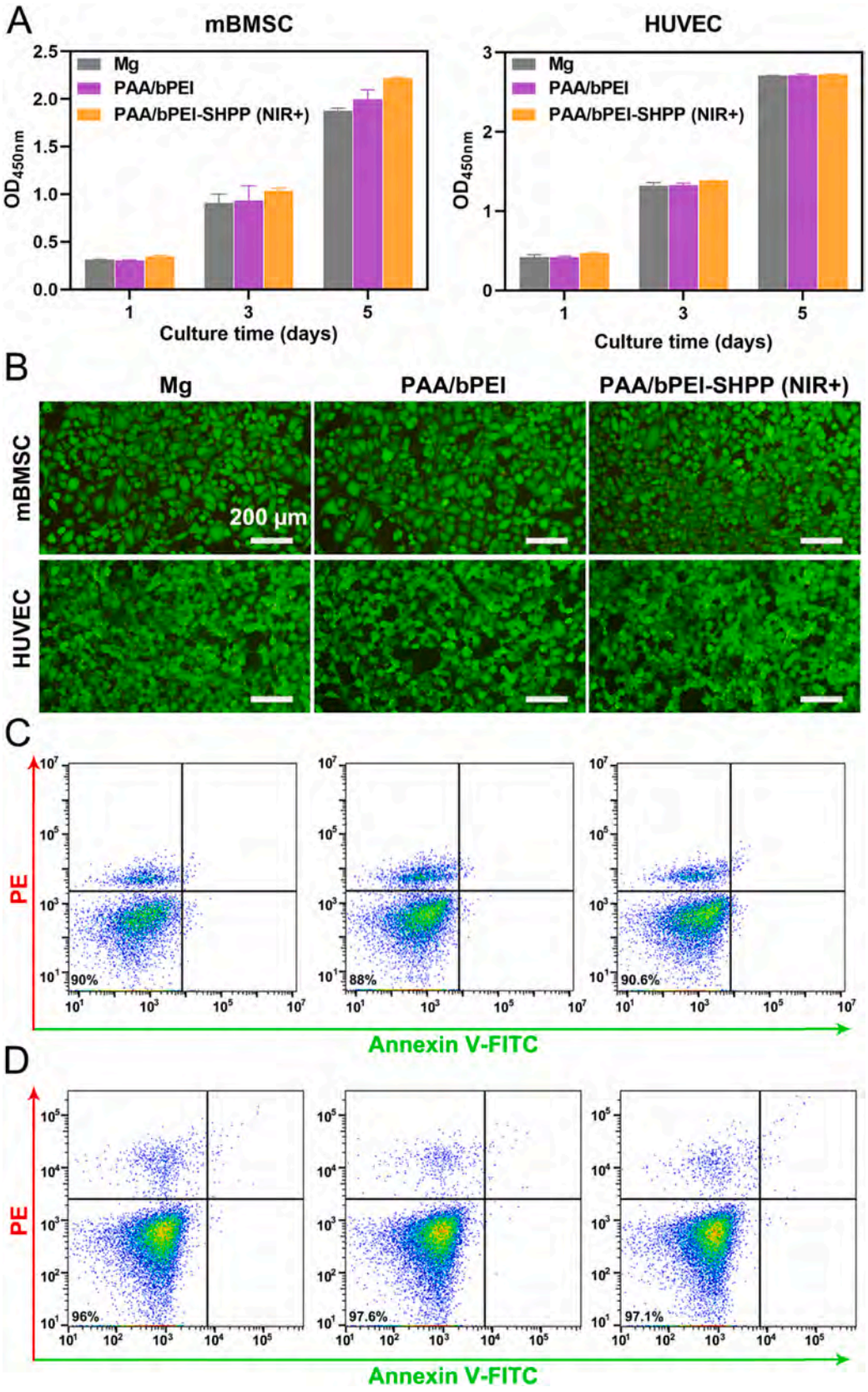

Fig. 10. *In vitro* cytocompatibility: (A) Cell proliferation evaluated by the CCK-8 assay for 1, 3 and 5 days. (B) Fluoroscopy images of live/dead (green/red) stained mBMSC and HUVEC treated with various samples. (C) mBMSC and (D) HUVEC apoptosis verified by Annexin V-FITC/7-AAD double staining and flow cytometry. (For interpretation of the references to colour in this figure legend, the reader is referred to the Web version of this article.)

magnitude decreasing from 14.86 to 6.97 kΩ cm^2. The wave diagrams of the EIS modulus impedance are acquired from ten repeated scratching and healing cycles. In EIS variation plot, each magnitude changes by more than one order of magnitude and $|Z|_{0.1Hz}$ still reaches 11.21 kΩ cm^2 after ten self-recovering steps. Hence, the PAA/bPEI-SHPP hybrid coating maintains eminent self-repairing properties and corrosion protection after several rounds of physical damage. The switchable damage-repair process ocurrs ten times in Fig. 6F. The water contact angle (CA) decreases slightly with increasing scratching-healing cycles, but still excceds 60°. After being covered with the nanocapsules-incorporated polymeric hybrid coating, the Mg/PAA/bPEI-SHPP coating shows water-enabled self-healing properties governed by the molecular mobility and chemical composition.

The self-healing mechanism of the scratched PAA/bPEI-SHPP coating is proposed and schematically illustrated in Fig. 6G and H. The PAA and bPEI molecules are employed as weak polyelectrolytes in the SSLbL assembly coating. Diffusion of the polyelectrolyte prompts the polymers in the self-assembled films to move quickly in response to environmental stimuli, thus polymer complexation in the coating may be suppressed [91,92]. The high mobility of polymer molecules leads to the formation of the polyelectrolyte multilayers (PEMs) with low hydrogen bonding and facilitates molecular diffusion in the formed PEMs. In Fig. 6G, the dynamic reversible chemical reactions between PAA and bPEI polyelectrolytes promote self-healing process when the LbL-assembled coating is immersed in an aqueous solution. In Fig. 6H, the water-enabled self-healing mechanism of the PAA/bPEI-SHPP hybrid coating includes two steps: (i) defect closure and (ii) defect sealing. Most of the large artificial scratches are closed by strong hydrogen and weak hydrogen is rebuilt between the broken PAA and bPEI molecules. The subtle cracks formed before are then sealed by the reversible amide reaction, restoring the original structure and functions of the polymeric hybrid coating.

The self-healing efficiency of the coated samples with 50 μm of wider scratches is evaluated by CLSM (Fig. 7), which can characterize the ultimate self-healing (USH) performance based on the changes of the scratched depth. The self-healing efficiency is calculated by the variation of the cutting depth. For the PAA/bPEI coating, the scratch is repaired after 5 h of immersion and the scratch depth decreases from 51.683 to 17.387 μm. The self-healing efficiency (η_{5h}) is about 66%. After healing on the PAA/bPEI-SHPP coating, the 56.928 μm deep scratch is filled with the coating materials to reach 11.559 μm, indicating that η_{5h} is about 80%. Therefore, the results indicate that the PAA/bPEI-SHPP coating possesses capacity to repair larger defects on Mg substrate.

3.6. Drug loading and release profiles

UV–vis spectrophotometry is utilized to measure the loading and leaching characteristics of SIM from the SHPP nanocontainers. The pure materials (SIM) and final products (SH, SHP and SHPP) are dispersed in homogeneous solutions in Fig. 8A. The UV–vis spectra display strong and broad absorbance of SHPP at 220–250 nm, suggesting its high potential as a photothermal agent. The typical absorbance peaks at 231, 239, and 248 nm are consistent with the absorption bands of free SIM at 230, 238, and 246 nm, respectively. The redshift arises from the formation of SIM dimers or oligomers, also known as J-aggregates. The extract of SHPP shows a positive correlation between absorbance and concentration, reflecting good dispersibility (Fig. 8B). The HMSs encapsulated with SIM exhibit the time- and dose-dependent cumulative drug loading behavior in Fig. 8C. By extending the incubation time from 2 to 12 h, the cumulative loading doses of SIM at 10, 20 and 50 mM significantly increase. The HMSs treated with 50 mM of SIM for 12 h have a maximum drug loading efficiency (DLE) of 44.01 ± 1.74% ($p < 0.05$) and this protocol is implemented throughout the experiments. Precise control and rapid response of drug release are crucial to antibacterial activity and bone regeneration. Controlled release of SIM from SHPP is particularly challenging in terms of the relatively low solubility in aqueous solutions and therefore the drug-loaded HMSs are functionalized with PDA and PCL-DA to improve the pH- and NIR-triggered drug-release mechanism.

Fig. 8D shows the drug release plots of SIM from the SH and SHPP dispersion at different pH values. When the pH of PBS is 7.4, the SHPP nanocapsules show only 8.30% drug release in the initial 12 h and then 20.55% and 44.59% SIM release in the 1st and 7th days. When the pH decreases to 5.5, the drug release rate increases significantly at all time, illustrating that the acid-triggered boost release of SIM from SHPP stems from the pH-responsive nature of PDA. The release rate of SIM from the SH dispersion at pH 5.5 or 7.4 is still higher than that from SHPP after incubation for 168 h, while about 82.52% SIM leaches from SH at pH 5.5. It may be caused by direct release of drugs from SH and rapid degradation of HMSs under acidic conditions. To visualize the light-triggered release mechanism, the SHPP extracts are illuminated by a 808 nm NIR laser with different densities (0.5, 1.0, and 2.0 W cm^{-2}) for 5 min at time points of 0, 1, 3, and 5 days, repsectively. The drug leached solutions are collected and irradiated for 1 h (NIR-remote period). Fig. 8E and F presents the NIR-triggered drug release behavior at pH 7.4 and 5.5 for different irradiation intensities. The release plots show obvious acceleration of SIM release at both pH values upon NIR illumination. Therefore, the SHPP nanocontainers prolong release of SIM and it can be controlled by the adjustment of pH and NIR (Fig. 8G).

3.7. Antibacterial assay

Given the sensitivity of the PAA/bPEI-SHPP hybrid coating, a 808 nm NIR laser is utilized to kill bacteria. The antibacterial capaticity is evaluated by culturing two types of pathogenic bacteria (*S. aureus* and *E. coli*) for 4 and 12 h, separately, and analyzed by a spread plate-counting method. After 4 h of incubation (Fig. 9A), the NIR-treated PAA/bPEI-SHPP coating shows higher antibacterial efficiency than that of the PAA/bPEI coating, indicating good inhibition effects against *S. aureus* and *E. coli*. The bacteria colonies on the bare Mg decrease sharply due to the released Mg^{2+} and increased pH during corrosion process. Compared to bare Mg, the PAA/bPEI coating demonstrates poorer antibacterial property but it offers a better barrier to Mg alloy. After 12 h of incubation, there are almost no live bacteria in these groups confirming the long-term antibacterial activity against *S. aureus* and *E. coli*.

In Fig. 9B, after the 808 nm NIR laser treatment, the PAA/bPEI-SHPP coating shows excellent bacteria-killing effects due to hyperthermia, reactive oxygen species (ROS), and the leached SIM (used as the sterilant). Under NIR laser irradiation, the PAA/bPEI-SHPP coating generates ROS and heat. It has been reported that both PTT and PDT can inhibit live gram positive and negative bacteria. In particular, thermotherapy destroys biofilms due to the generation of ROS and hyperthermia, thereby promoting carrier migration. ROS react with membranes through various mechanisms, producing membrane rupture, protein leaching, and even damage of DNA and organelles. Meanwhile, thermally triggered release of SIM from the PAA/bPEI-SHPP coating can inhibit bacterial infections.

3.8. Cytocompatibility

The *in vitro* cytocompatibility of bare Mg, the PAA/bPEI and PAA/bPEI-SHPP coatings incubated with mBMSC and HUVEC is assessed by CCK-8 assay, live/dead staining, and flow cytometry. The viability of both cells enhances with incubation time (Fig. 10A) indicating that the NIR-treated PAA/bPEI-SHPP coating is noncytotoxic and even helps to promote cell proliferation of mBMSC *in vitro*. HUVECs have the potential of stem cells and have been confirmed to secrete BMP, which can motivate osteogenic differentiation and stimulate osteoblasts and precursor cells to secrete VEGF. The BMP-2 and VEGF are essential for new bone formation in addition to fast endothelization for cytocompatibility

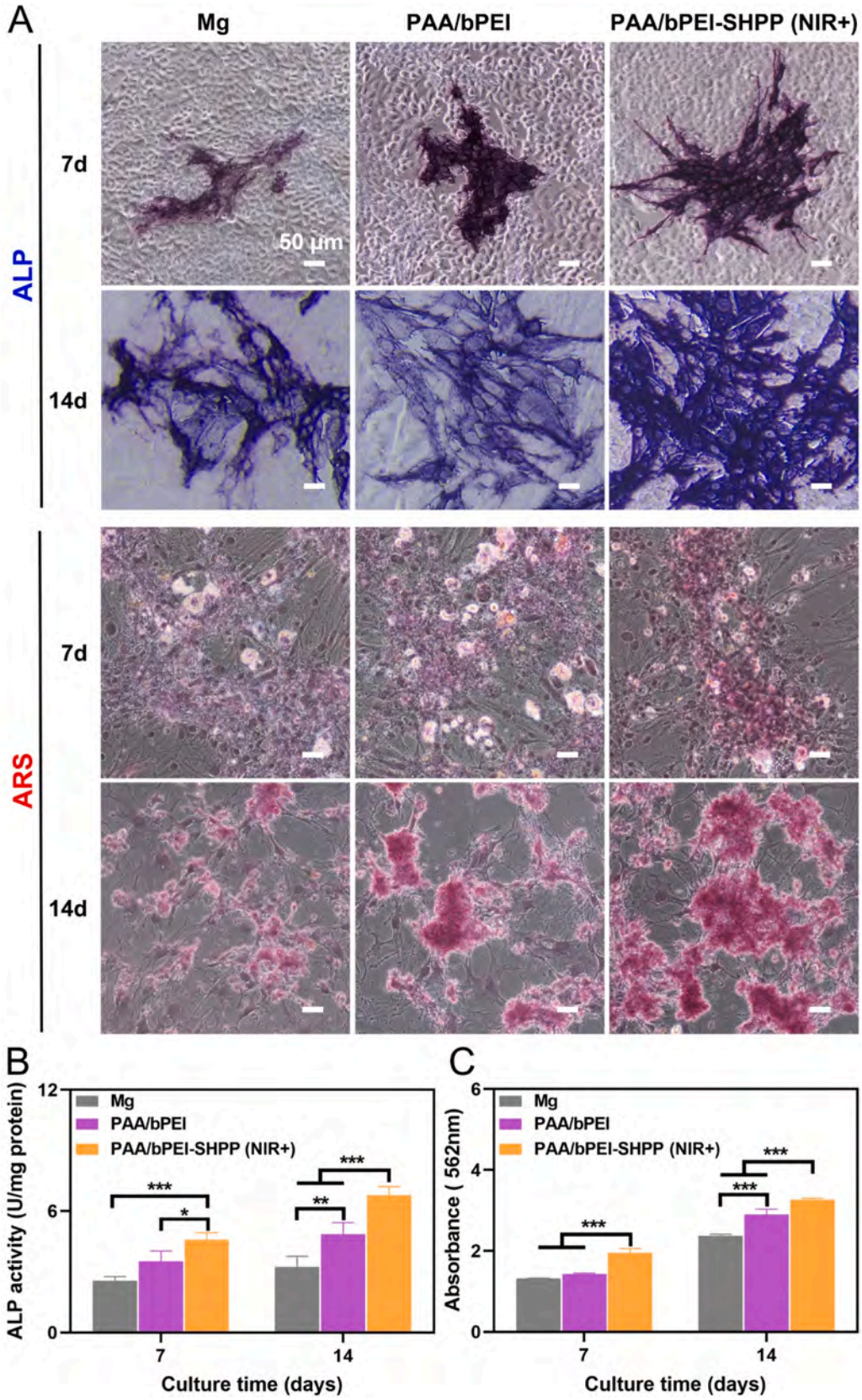

Fig. 11. *In vitro* evaluation of osteogenesis: (A) ALP and Alizarin Red staining of mBMSC cultured in extracts of the various samples for 7 and 14 days. (B) Qualitative ALP activities. (C) Quantitative ECM mineralization of mBMSC. $^{*}p < 0.05$, $^{**}p < 0.01$ and $^{***}p < 0.001$. (For interpretation of the references to colour in this figure legend, the reader is referred to the Web version of this article.)

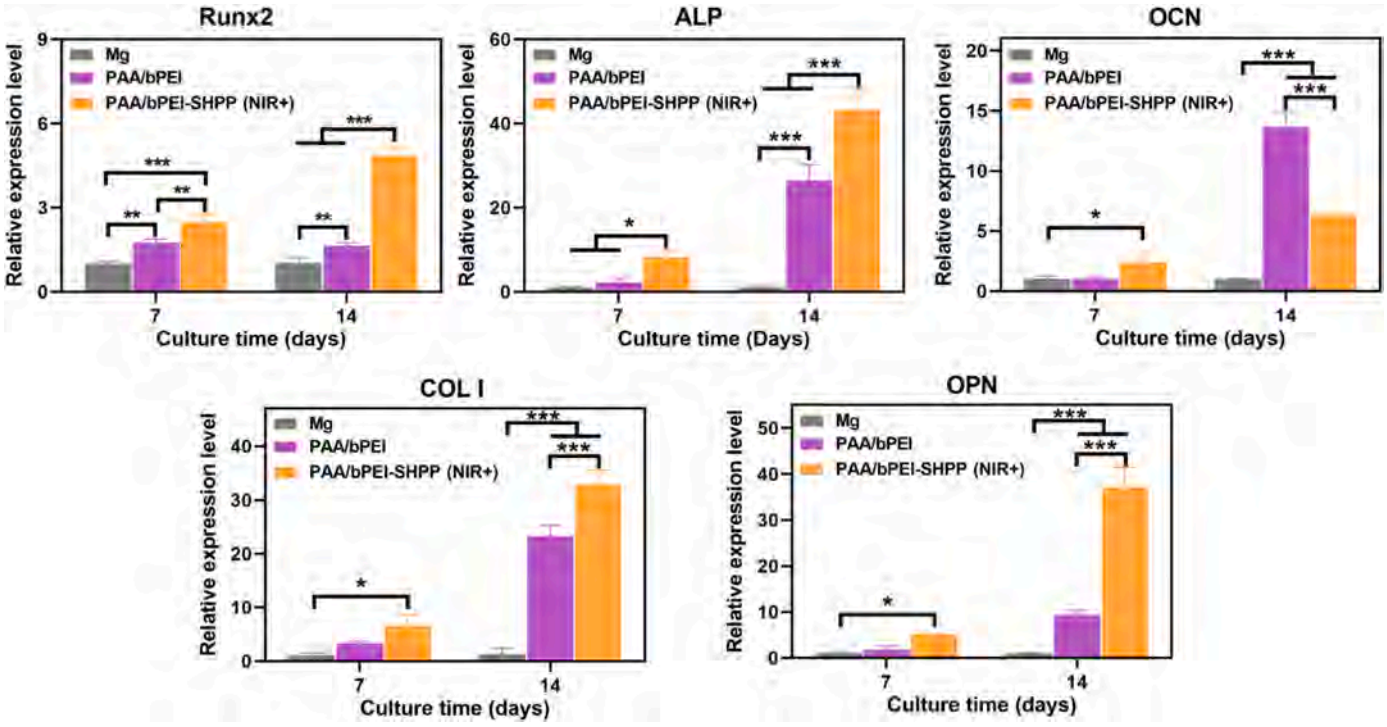

Fig. 12. Relative mRNA expression. Some osteogenic differentiation genes Runx2, ALP, OCN, COL I and OPN of the mBMSCs were cultured on the various samples for 7 and 14 days. $^{*}p < 0.05$, $^{**}p < 0.01$ and $^{***}p < 0.001$.

in vitro. After 1, 3 and 5 days of culture in extracts of Mg alloy, PAA/bPEI, and PAA/bPEI-SHPP (NIR+), proliferation of HUVECs on these samples is evaluated and the results reveal little difference in the viability of HUVECs.

The cell viability on all the specimens increases with time. In Fig. 10B, the live/dead cell stained images of mBMSC and HUVEC show no obvious dead cells. The typical stem cell morphology is observed and the distribution is uniform and healthy. Therefore, SHPP incorporation and NIR irradiation hardly influence the compatibility between PAA/bPEI-SHPP hybrid coating and mBMSC/HUVEC cells. Flow cytometry is conducted to further evaluate the effects of the PAA/bPEI-SHPP coating on cell apoptosis. In Fig. 10C, the ratio of mBMSC cells in the Q3 area of the PAA/bPEI-SHPP coating reaches 90.6%, which is 0.6% and 2.6% higher than those of bare Mg and the PAA/bPEI coating. Moreover, the ratios of normal HUVEC living cells (Fig. 10D) of the three samples are higher than 96%, so that cells can grow adequately in the extracts. The results prove that the NIR-treated PAA/bPEI-SHPP coating has negative effects on cell apoptosis and good cytocompatibility *in vitro*.

3.9. Osteogenesis assay

Osteogenesis determines the potential therapeutic outcome after implant surgery. Alkaline phosphatase (ALP) as the residual product of osteoblast activity is considered an initial indicator of osteogenic differentiation and a higher APL level reflects the formation of bioactive bone. Among the three specimens, the NIR-irradiated PAA/bPEI-SHPP coating shows the highest and most compact ALP positive staining (Fig. 11A) for the enhanced ALP activity (Fig. 11B) after being cultured for 7 and 14 days, respectively. ECM mineralization is important to osteogenic differentiation in the final stage and mainly mediated by osteoblasts. Alizarin red staining of mBMSCs indicates that the mineralization level of ECM in the NIR-irradiated PAA/bPEI-SHPP coating is higher than that of the other specimens. According to the quantitative results (Fig. 11C), formation of mineralized nodules in the SHPP-incorporated polymeric coating (NIR+) is about 1.4 and 2.1 times greater than those on the bare Mg alloy and PAA/bPEI coating, and the difference is actually significant ($p < 0.001$). Hence, the NIR-irradiated PAA/bPEI-SHPP coating accelerates osteogenic differentiation of mBMSCs by promoting the cells to a mature phenotype and expediting ECM mineralization giving rise to the pronounced improvements *in vitro*.

After incubation for 7 and 14 days, the expression levels of osteogenic-related genes in the mBMSC cells are evaluated by RT-PCR. In Fig. 12, the mBMSC cells cultured on the PAA/bPEI-SHPP (NIR+) specimen exhibit the highest expression of Runx2, ALP, COL I and OPN on the 7th and 14th day. The relative expression levels of ALP, COL I and OPN of the PAA/bPEI-SHPP coating increase by several dozen times compared to the control (Mg alloy) after 14 days. The mRNA levels of Runx2 and OCN in the SHPP-contained hybrid coating are 4.2 and 6.18 folds higher than in Mg substrate after 14 days, demonstrating that the NIR-treated PAA/bPEI-SHPP coating is favorable to cell proliferation, osteogenesis, and differentiation of osteoblasts.

3.10. Effect of surface roughness on osteoblasts

The surface characteristics of implants are key factors in bone response to metallic bone implants [93]. Studies have confirmed that the surface roughness of biomaterials plays a key role in the early adhesion and differentiation of osteoblasts [94–97]. In Fig. 13A and B, the surface of the bare Mg showes a nanoscale roughness with a Ra value of 40.3 nm, while the values of PAA/bPEI and PAA/bPEI-SHPP (NIR+) are 19.5 and 21.7 nm, respectively, demonstrating that the surface modification can significantly improve the surface roughness of bare Mg substrate. We further investigates the cell-scaffold integration behaviors after 24 h of culture by using SEM analysis in Fig. 13C. The well-expanded cytoskeleton of mBMSCs cells on the three different surfaces, the formation of pseudopodia, and the pronounced spreading on the sample surfaces indicates that the osteoblasts are tightly attached. The mBMSCs possess both two- and three-dimensional structures, with numerous cell-to-cell interactions able to be clearly visualized. However, different coverage percentages and distribution characteristics of cells are observed on the three sample surfaces. Compared with the bare Mg, the two coated samples with lower surface roughness have a bigger cell coverage area.

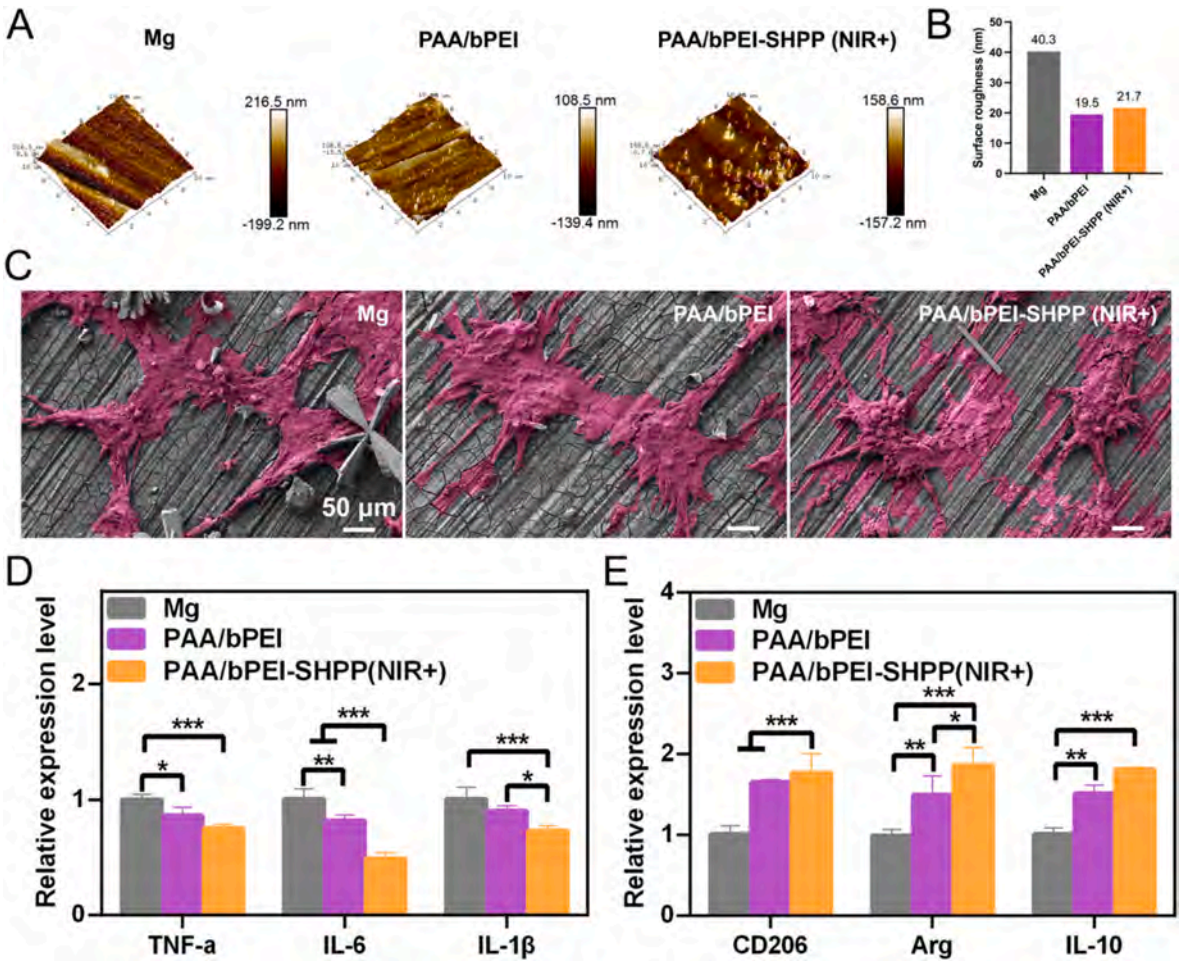

Fig. 13. Relationship between surface roughness and osteogenesis activity, and relative RNA expression of immune-related genes. (A) AFM images of different samples. (B) The corresponding surface roughness of materials in Fig. A. (C) SEM morphologies of mBMSCs on different samples after incubation for 24 h. (D) M1-type macrophages polarization-related genes (TNF-α, IL-6, and IL-1β) and (E) M2-type macrophages polarization-related genes (CD206, Arg, and IL-10) were cultured with the various specimens for 3 days. $*p < 0.05$, $**p < 0.01$, and $***p < 0.001$.

Especially on the surface of PAA/bPEI-SHPP (NIR+) group, the mBMSCs have more prominent protrusions and circular nuclei. Therefore, the surface modification could reduce the surface roughness of bare Mg, thus effectively boosting the cell adhesion and osteogenic differentiation.

3.11. Macrophage polarization in vitro

The polarization behaviors of RAW264.7 macrophages are measured in this study. After 3 days of incubation, the total RNA is extracted for reverse transcription, and qPCR is used to detect relative genes in macrophages. Studies proposed that M1 can promote the increase of osteoclast precursors or directly facilitate the differentiation of macrophage-induced osteoclast precursors into osteoclasts by secreting a variety of cytokines (such as TNF-α, IL-6, and IL-1β) [98–101]. This study shows that the PAA/PEI-SHPP (NIR+) group (Fig. 13D) can inhibit the release of TNF-α, IL-6 and IL-1β from M1 cells and the differentiation of macrophages into osteoclasts, and thus promote osteogenesis through co-culture of extract solution. Macrophage M2 features the high expression of CD206 and secretion of anti-inflammatory cytokines, such as IL-10, Arg-1, and TGF-β1, inhibites the development of inflammation, and promotes inflammation regression and tissue repair [102]. The IL-10 is a potent anti-inflammatory factor produced primarily by M2 that inhinites osteoclast differentiation in the early stage of osteoclast formation [100]. The results in Fig. 13E suggest that the secretion of CD206, Arg, and IL-10 in M2 cells are significantly increased, thus PAA/bPEI-SHPP (NIR+) coating has the potential to induce bone immunity and promote tissue repair.

3.12. Angiogenesis assay

HUVEC Migration is essential for recovery after vascular injury and cell recruitment is performed by the scratch test and transwell assay *in vitro*. The number of migrated HUVECs in the PAA/bPEI-SHPP (NIR+) group increases significantly in the wound healing assay (Fig. 14A and C). In the transwell assays (Fig. 14B and D), the SHPP-incorporated hybrid coating also shows a higher number of traversing cells than the other groups *in vitro*. The vascular endothelial growth factor (VEGF) is an important cytokine for the vascular network and the expression of VEGF in the HUVEC cells is shown in Fig. 14E. Compared with the other groups, the PAA/bPEI-SHPP (NIR+) sample increases VEGF protein production on day 1 and 3. VEGF shows high specificity to HUVECs and its continuous secretion improves the angiogenesis activity of endothelial cells. The hypoxia inducible factor α (HIF-α) regulates the expression of VEGF at the genetic level and is also a considerable regulator of angiogenesis. In Fig. 14F, the expression of HIF-α increases significantly in the PAA/bPEI-SHPP (NIR+) group compared with other specimens.

3.13. In vivo experiments

In this study, a bone-implant model with femoral condylar defects is constructed to further validate the osteointegration capacity *in vivo*. The

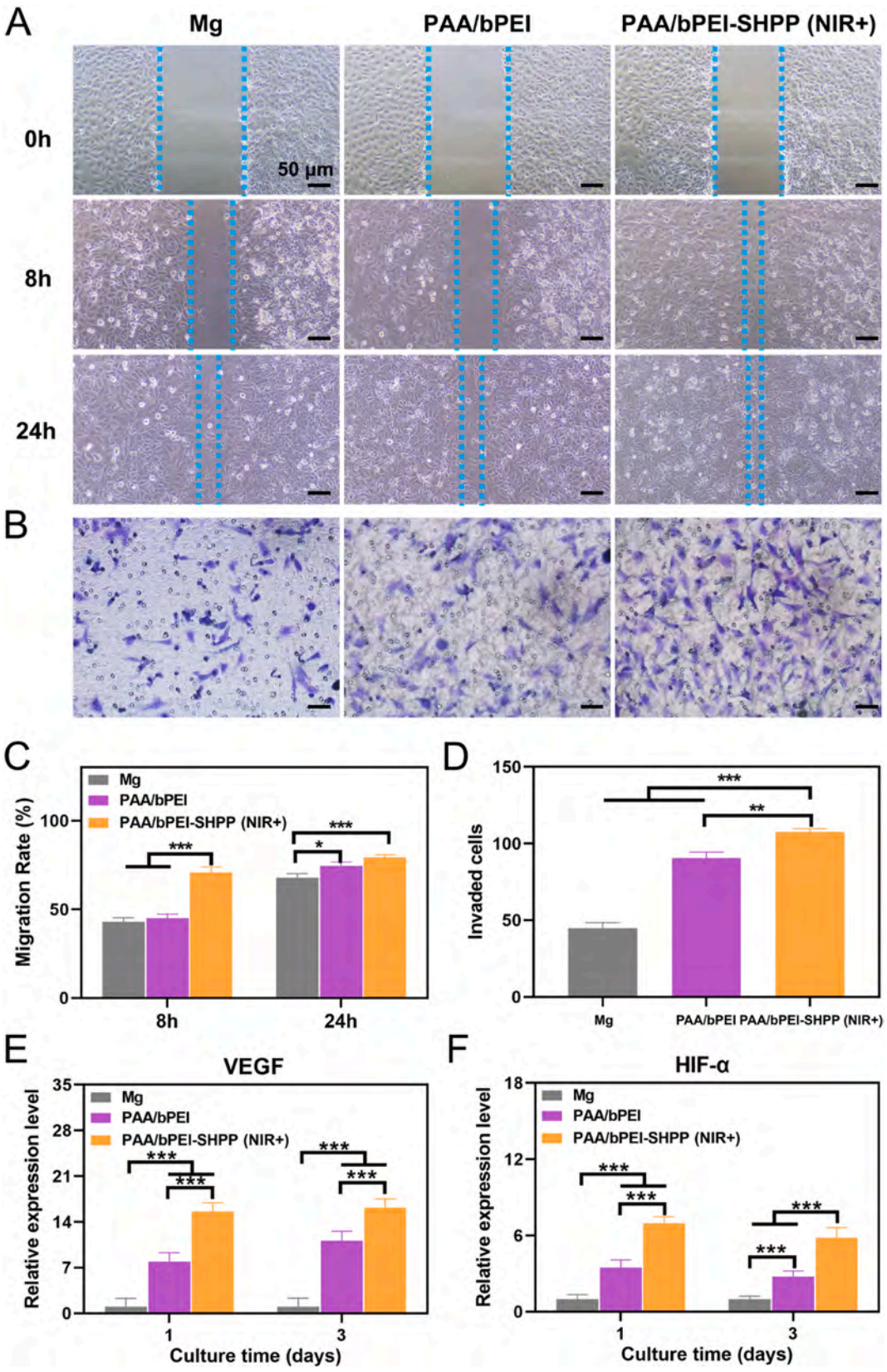

Fig. 14. Angiogenic ability of HUVECs: (A) Migration of HUVECs cultured for 8 and 24 h with the quantitative results shown in (C); (B) Stained migrating HUVCEs cultured for 12 h in the transwell assay with the number of invading cells shown in (D). Relative mRNA expression of angiogenic-related genes: (E) VEGF and (F) HIF-α for HUVEC cultured in the extracts of various samples for 1 and 3 days. $^{*}p < 0.05$, $^{**}p < 0.01$, and $^{***}p < 0.001$.

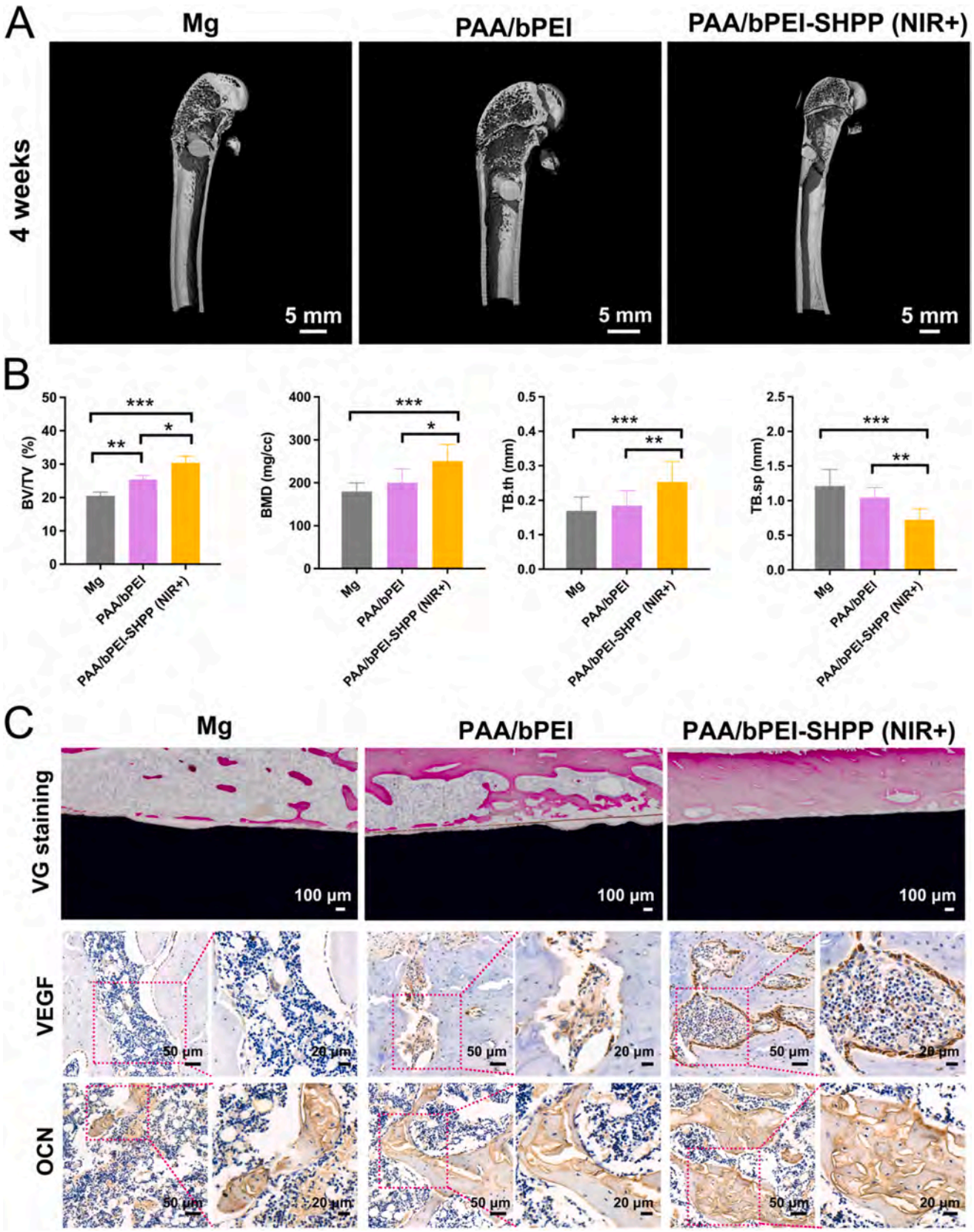

Fig. 15. *In vivo* evaluation of osteogenesis. (A) Micro-CT evaluation of bone regeneration of the femoral condyle defects after implantation for 4 weeks. (B) Quantitative analysis of osteogenesis effect of samples 4 weeks after operation from BV/TV, BMD, TB. th, and TB. sp. (C) VG, VEGF, and OCN immunostaining of the specimens after femur implantation for 4 weeks. $^{*}p < 0.05$, $^{**}p < 0.01$, and $^{***}p < 0.001$.

same standard-sized pillars are used as implants in rabbit femurs. At week 4 after implantation with the three different columns, the bone tissue with the implant is harvested. The micro-CT is performed to estimate the osteogenesis property (Fig. 15A). The coronal plane of the femoral condyle is investigated, and three-dimensional reconstruction is performed to evaluate the healing process and new bone volume. The osteogenesis of the PAA/bPEI-SHPP (NIR+) group is better than the bare Mg and PAA/bPEI groups. For cylindrical implant areas, the BV/TV, BMD, Tb. th, and Tb. sp data of the three different materials are analyzed and compared as shown in Fig. 15B. The PAA/bPEI-SHPP (NIR+) group shows the highest BV/TV, BMD, and Tb. th values, as well as the lowest Tb. sp value, revealing the best osteogenesis and osteoinductivity, with the enhanced formation and thickening of new bone tissues. It can be interpreted by the fact that the loaded simvastatin promotes the osteogenic differentiation of BMSCs [103–106]. In addition, the combination of degradation-produced Mg^{2+} and the released simvastatin significantly mitigates the trabecular bone loss by preventing osteoclast formation and bone resorption [107].

The bone around the implant is red-stained by Van Gieson (VG) staining for the undecalcified sections in Fig. 15C. Only a few new bone tissues surround the bare Mg implant, which are not tightly bounded to the substrate. On the contrary, the completed new bone circles are formed in PAA/bPEI-SHPP (NIR+) pillar, and the new bone is thicker and more connected than those in the other two groups. Furthermore, immunohistochemical staining for the special marker (osteocalcin, OCN) of osseointegration is performed on the decalcified histological sections. After 4 weeks implantation, compared with the Mg implants, larger staining areas and deeper positive staining are observed around the both two coated samples. Especially, the PAA/bPEI-SHPP (NIR+) group displays the most OCN expression during the bone reconstruction around the implants. In addition, the PAA/bPEI-SHPP (NIR+) implant enhances the gene expression of pro-angiogenic factor VEGF, which contributes to the construction of a pro-angiogenic biochemical microenvironment. Therefore, the results prove that the PAA/bPEI-SHPP (NIR+) coating effectively promotes *in vivo* osseointegration.

4. Conclusion

A defect-free and smooth self-healing hybrid coating composed of stimuli-responsive nanocontainers is prepared on biodegradable Mg alloys by a spin-spray layer-by-layer assembly method to accomplish bacteria killing, osteogenesis, and angiogenesis synergistically.

(1) The PAA/bPEI-SHPP coating possesses excellent photothermal conversion capacity and photostability. Electrochemical and immersion measurements confirm that the hybrid coating protects the Mg substrate from corrosion in HBSS up to 240 h.
(2) The high mobility of PAA and bPEI polyelectrolytes, dynamic reversible hydrogen bonding, and amide bond interactions fosters the water-enabled self-healing behavior in a rapid, stable, and repetitive manner.
(3) The antibacterial assay demonstrates favorable bacteria-killing properties under NIR irradiation as a result of synergistic hyperthermia, reactive oxygens species, and SIM leaching.
(4) In the PAA/bPEI-SHPP coating, the incorporated SHPP nanocontainers prolong release of simvastatin, which can be controlled by pH and photothermal stimuli.
(5) The NIR-irradiated surface shows improved cytocompatibility, accelerated osteogenesis differentiation and vascular endothelial angiogenesis, and enhanced alkaline phosphatase activity. The extracellular matrix mineralization and expression of osteogenesis-related genes are also expedited.

Credit author statement

Yanbin Zhao: Conceptualization, Methodology, Software, Formal analysis, Writing -original draft, Writing - review & editing. **Peng He:** Data curation, Validation, Investigation. **Junyan Yao:** Investigation, Visualization, Software. **Mei Li:** Conceptualization, Methodology, Writing - review & editing. **Bin Wang:** Investigation. **Linyuan Han:** Software. **Zhihai Huang:** Resources. **Chao Guo:** Resources. **Jing Bai:** Resources. **Feng Xue:** Resources. **Yu Cong:** Resources. **Weihua Cai:** Resources, Writing - review & editing. **Paul K. Chu:** Resources, Writing - review & editing. **Chenglin Chu:** Conceptualization, Supervision, Project administration.

Declaration of competing interest

The authors declare that they have no known competing financial interests or personal relationships that could have appeared to influence the work reported in this paper.

Data availability

Data will be made available on request.

Acknowledgements

This work was supported by the National Natural Science Foundation of China (grant numbers 52171236, 51971062), Open Research Fund of Jiangsu Key Laboratory for Advanced Metallic Materials, Southeast University (grant number AMM2021A01), General Fund of Scientific Research Project of Jiangsu Provincial Health Commission (grant number H2019022), City University of Hong Kong Strategic Research Grant (SRG) (grant number 7005505), as well as City University of Hong Kong Donation Research Grant (grant number DON-RMG 9229021).

References

[1] S. Amukarimi, M. Mozafari, Biodegradable magnesium biomaterials-road to the clinic, Bioengineering 9 (2022) 107.
[2] Y. Zhang, J. Xu, Y.C. Ruan, M.K. Yu, M. O'Laughlin, H. Wise, D. Chen, L. Tian, D. Shi, J. Wang, Implant-derived magnesium induces local neuronal production of CGRP to improve bone-fracture healing in rats, Nat. Med. 22 (2016) 1160–1169.
[3] O. Suljevic, S.F. Fischerauer, A.M. Weinberg, N.G. Sommer, Immunological reaction to magnesium-based implants for orthopedic applications. What do we know so far? A systematic review on in vivo studies, Mater. Today Bio 15 (2022), 100315.
[4] Y. Liu, Y.F. Zheng, X.H. Chen, J.A. Yang, H.B. Pan, D.F. Chen, L.N. Wang, J. L. Zhang, D.H. Zhu, S.L. Wu, K.W.K. Yeung, R.C. Zeng, Y. Han, S.K. Guang, Fundamental theory of biodegradable metals-definition, criteria, and design, Adv. Funct. Mater. 29 (2019), 1805402.
[5] M. Ebrahimi, Q.D. Wang, S. Attarilar, A comprehensive review of magnesium-based alloys and composites processed by cyclic extrusion compression and the related techniques, Prog. Mater. Sci. 131 (2023), 101016.
[6] L.Y. Li, Z. Yang, X.X. Pan, B.X. Feng, R. Yue, B. Yu, Y.F. Zheng, J.Y. Tan, G. Y. Yuan, J. Pei, Incorporating copper to biodegradable magnesium alloy vascular stents via a Cu(II)-Eluting coating for synergistic enhancement in prolonged durability and rapid Re- endothelialization, Adv. Funct. Mater. 29 (2022), 2205634.
[7] X. Li, C.L. Chu, L. Liu, X.K. Liu, J. Bai, C. Guo, F. Xue, P.H. Lin, P.K. Chu, Biodegradable poly-lactic acid based-composite reinforced unidirectionally with high- strength magnesium alloy wires, Biomaterials 49 (2015) 135–144.
[8] J.W. Dai, C.Q. Wu, J.Y. Yang, L. Zhang, Q.S. Dong, L.Y. Han, X. Li, J. Bai, F. Xue, P.K. Chu, C.L. Chu, Poly-lactic acid coatings on the biomedical WE43 Mg alloy: protection mechanism and ion permeation effects, Prog. Org. Coating 177 (2023), 107427.
[9] M. Kavyani, G.R. Ebrahimi, H.R. Ezatpour, M. Jahazi, Microstructure refinement, mechanical and biocorrosion properties of Mg–Zn–Ca–Mn alloy improved by a new severe plastic deformation process, J. Magnes. Alloy. 10 (2022) 1640–1662.
[10] M. Esmaily, J.E. Svensson, S. Fajardo, N. Birbilis, G.S. Frankel, S. Virtanen, R. Arrabal, S. Thomas, L.G. Johansson, Fundamentals and advances in magnesium alloy corrosion, Prog. Mater. Sci. 89 (2017) 92–193.
[11] L.J. He, Y. Shao, S.Q. Li, L.Y. Cui, X.J. Ji, Y.B. Zhao, R.C. Zeng, Advances in layer-by- layer self-assembled coatings upon biodegradable magnesium alloys, Sci. China Mater. 64 (2021) 2093–2106.
[12] J.L. Wang, J.K. Xu, C. Hopkins, D.H. Chow, L. Qin, Biodegradable Magnesium ased implants in orthopedics-A general review and perspectives, Adv. Sci. 7 (2020), 1902443.
[13] K. Xie, N.Q. Wang, Y. Guo, S. Zhao, J. Tan, L. Wang, G.Y. Li, J.X. Wu, Y.Z. Yang, W.Y. Xu, Additively manufactured biodegradable porous magnesium implants for

elimination of implant-related infections: an in vitro and in vivo study, Bioact. Mater. 8 (2022) 140–152.
[14] B. Li, R. Huang, J. Ye, L. Liu, L. Qin, J.H. Zhou, Y.F. Zheng, S.L. Wu, Y. Han, A self- healing coating containing curcumin for osteoimmunomodulation to ameliorate osseointegration, Chem. Eng. J. 403 (2020), 126323.
[15] W.J. Huang, D. Mei, H.T. Qin, J.G. Li, L.G. Wang, X.S. Ma, S.J. Zhu, S.K. Guan, Electrophoretic deposited boron nitride nanosheets-containing chitosan-based coating on Mg alloy for better corrosion resistance, biocompatibility and antibacterial properties, Colloid. Surface. A 638 (2022), 128303.
[16] Y. Zhang, J. Cao, M.M. Lu, Y. Shao, K.W. Jiang, X.D. Yang, X.Y. Xiong, S. Wang, C. L. Chu, F. Xue, Y.J. Ye, J. Bai, A biodegradable magnesium surgical staple for colonic anastomosis: in vitro and in vivo evaluation, Bioact. Mater. 22 (2023) 225–238.
[17] H.H. Du, D.D. Zhang, R. Xu, J.N. Xie, S.W. Guan, S.H. Chen, F. Peng, S. Qian, X. Y. Liu, Ferric oxide nanosheet-engineered Mg alloy for synergetic osteosarcoma photothermal/chemodynamic therapy, J. Mater. Sci. Technol. 138 (2023) 203–213.
[18] K.T. Kotoulas, J. Campbell, A.G. Skirtach, D. Volodkin, A. Vikulina, Surface modification with particles coated or made of polymer multilayers, Pharmaceutics 14 (2022) 2483.
[19] T. Kruka, K.C. Górka, M.K. Sojkaa, S. Zapotoczny, Stimuli-responsive polyelectrolyte multilayer films and microcapsules, Adv. Colloid Interfac. 310 (2022), 102773.
[20] D. Alkekhia, P.T. Hammond, A. Shukla, Layer-by-Layer biomaterials for drug delivery, Annu. Rev. Biomed. Eng. 22 (2020) 1–24.
[21] Z.Y. Zhang, J.F. Zeng, J. Groll, M. Matsusaki, Layer-by-layer assembly methods and their biomedical applications, Biomater. Sci. 10 (2022) 4077–4094.
[22] J.J. Richardson, J. Cui, M. Bjornmalm, J.A. Braunger, H. Ejima, F. Caruso, Innovation in layer-by-layer assembly, Chem. Rev. 116 (2016) 14828–14867.
[23] J.Y. Yang, Y.B. Zhao, J.W. Dai, L.Y. Han, Q.S. Dong, L. Zhang, J. Bai, F. Xue, P. K. Chu, C.L. Chu, Fabrication and growth mechanism of multilayered hydroxyapatite/organic composite coatings on the WE43 magnesium alloy, Surf. Coat. Technol. 452 (2023), 129125.
[24] Y.B. Zhao, X.Y. Chen, S.Q. Li, R.C. Zeng, F. Zhang, Z.L. Wang, S.K. Guan, Corrosion resistance and drug release profile of gentamicin-loaded polyelectrolyte multilayers on magnesium alloys: effects of heat treatment, J. Colloid Interf. Sci. 547 (2019) 309–317.
[25] Z. Xiao, L.H. Liu, T. Liu, D. Yang, X. Jia, Y.K. Du, S.Q. Li, W.J. Yang, Y.M. Xi, R. C. Zeng, Degradation and biocompatibility of genipin crosslinked polyelectrolyte films on biomedical magnesium alloy via layer-by-layer assembly, Prog. Org. Coating 175 (2023), 107372.
[26] Y.B. Zhao, L.Q. Shi, X.J. Ji, J.C. Li, Z.Z. Han, S.Q. Li, R.C. Zeng, F. Zhang, Z. L. Wang, Corrosion resistance and antibacterial properties of polysiloxane modified layer-by-layer assembled self-healing coating on magnesium alloy, J. Colloid Interf. Sci. 526 (2018) 43–50.
[27] S.K. Yang, R.X. Sun, K.Z. Chen, Self-healing performance and corrosion resistance of phytic acid/cerium composite coating on microarc-oxidized magnesium alloy, Chem. Eng. J. 428 (2021), 131198.
[28] L. Huang, J. Li, W. Yuan, X.M. Liu, Z.Y. Li, Y.F. Zheng, Y.Q. Liang, S.L. Zhu, Z. D. Cui, X.J. Yang, K.W.K. Yeung, S.L. Wu, Near-infrared light controlled fast self-healing protective coating on magnesium alloy, Corros. Sci. 163 (2020), 108257.
[29] J.X. Yang, D. Wang, J.H. Wang, W.B. Hu, Corrosion resistance and near-infrared light induced self-healing behavior of polycaprolactone coating with MIL-53@TA on magnesium alloy, Appl. Surf. Sci. 585 (2022), 152729.
[30] Y.L. Wu, L. Wu, W.H. Yao, Y.H. Chen, Y. Zhou, L.Q. Wang, T. Wu, B. Jiang, A. Atrens, F.S. Pan, ZnAl-LDH@MXene modified by inhibitor as a nanofiller applied on Mg alloys coating protection, Carbon 204 (2023) 36–49.
[31] A.S. Gnedenkov, S.L. Sinebryukhov, V.S. Filonina, N.G. Plekhova, S. V. Gnedenkov, Smart composite antibacterial coatings with active corrosion protection of magnesium alloys, J. Magnes. Alloy. 10 (2022) 3589–3611.
[32] J.K.E. Tan, N. Birbilis, S. Choudhary, S. Thomas, P. Balan, Corrosion protection enhancement of Mg alloy WE43 by in-situ synthesis of MgFe LDH/citric acid composite coating intercalated with 8HQ, Corros. Sci. 205 (2022), 110444.
[33] S.Q. Liu, Z.X. Li, Q.L. Yu, Y.M. Qi, Z.J. Peng, J. Liang, Dual self-healing composite coating on magnesium alloys for corrosion protection, Chem. Eng. J. 424 (2021), 130551.
[34] L. Cai, X. Song, C.B. Liu, L.Y. Cui, S.Q. Li, F. Zhang, M. Bobby Kannan, D.C. Chen, R.C. Zeng, Corrosion resistance and mechanisms of Nd(NO(3))(3) and polyvinyl alcohol organic-inorganic hybrid material incorporated MAO coatings on AZ31 Mg alloy, J. Colloid Interf. Sci. 630 (2023) 833–845.
[35] X.J. Li, Z.Y. Xue, W.T. Sun, J.H. Chu, Q.J. Wang, L.B. Tong, K.S. Wang, Bio-inspired self-healing MXene/polyurethane coating with superior active/passive anticorrosion performance for Mg alloy, Chem. Eng. J. 454 (2023), 140187.
[36] Q. Li, X.D. Zhang, S. Ben, Z.H. Zhao, Y.Z. Ning, K.S. Liu, L. Jiang, Bio-inspired superhydrophobic magnesium alloy surfaces with active anti-corrosion and self-healing properties, Nano Res. 16 (2022) 3312–3319.
[37] T. Wang, W. Wang, H.M. Feng, T.X. Sun, C.C. Ma, L. Cao, X.D. Qin, Y. Lei, J. M. Piao, C. Feng, Q.L. Cheng, S.G. Chen, Photothermal nanofiller-based polydimethylsiloxane anticorrosion coating with multiple cyclic self-healing and long-term self-healing performance, Chem. Eng. J. 446 (2022), 137077.
[38] D.D. Chen, M.D. Wu, B.C. Li, K.F. Ren, Z.K. Cheng, J. Ji, Y. Li, J.Q. Sun, Layer-by-layer-assembled healable antifouling films, Adv. Mater. 27 (2015) 5882–5888.
[39] G. Cui, Z.X. Bi, S.H. Wang, J.G. Liu, X. Xing, Z.L. Li, B.Y. Wang, A comprehensive review on smart anti-corrosive coatings, Prog. Org. Coating 148 (2020), 105821.
[40] K. Manabe, E. Koyama, Y. Norikane, Cephalopods-Inspired rapid self-healing nanoclay composite coatings with oxygen barrier and super-bubble-phobic properties, ACS Appl. Mater. Interfaces (2021) 36341–36349.
[41] Y.Q. Gu, N.S. Zacharia, Self-healing actuating adhesive based on polyelectrolyte multilayers, Adv. Funct. Mater. 25 (2015) 3785–3792.
[42] D.W. Grainger, H.C. Mei, P.C. Jutte, J.J.A.M. Dungen, H.J. Busscher, B.F.A. M. Laan, S.A.J. Zaat, H.J. Busscher, Critical factors in the translation of improved antimicrobial strategies for medical implants and devices, Biomaterials 34 (2013) 9237–9243.
[43] B.L. Tao, W.K. Zhao, C.C. Lin, Z. Yuan, Y. He, L. Lu, M.W. Chen, Y. Ding, Y. L. Yang, Z.Z. Xia, K.Y. Cai, Surface modification of titanium implants by ZIF-8@ Levo/LBL coating for inhibition of bacterial-associated infection and enhancement of in vivo osseointegration, Chem. Eng. J. 390 (2020), 124621.
[44] D.D. Zhang, F. Peng, J. Tan, Y. Zhang, F. Wang, J.N. Xie, R. Xu, H.H. Du, S. Qian, Y.Q. Qiao, M. Li, X.Y. Liu, Self-assembled ferric oxyhydroxide nanosheet on PEO-coated magnesium alloy with photocatalytic/photothermal antibacterial and enhanced osteogenesis activities, Chem. Eng. J. 437 (2022), 135257.
[45] J.W. Costerton, P.S. Greenberg, E.P. Greenberg, Bacterial biofilms: a common cause of persistent infections, Science 284 (1999) 1318.
[46] H.J. Maier, S. Julmi, S. Behrens, C. Klose, A.K. Gartzke, P. Wriggers, A. C. Waselau, A. Meyer-Lindenberg, Magnesium alloys for open-pored bioresorbable implants, Jom 72 (2020) 1859–1869.
[47] S.A. Abbah, C. Lam, D.W. Hutmacher, J. Goh, H.K. Wong, Biological performance of a polycaprolactone-based scaffold used as fusion cage device in a large animal model of spinal reconstructive surgery, Biomaterials 30 (2009) 5086–5093.
[48] Y.F. Zheng, X. Liu, D.N. Shen, W.T. Li, Y. Cheng, M. Yang, Y.H. Kou, B.G. Jiang, Perceiving the connection between the bone healing process and biodegradation of biodegradable metal implants through precise bioadaptability principle, J. Mater. Sci. Technol. 147 (2023) 132–144.
[49] L. Zhong, Y. Qu, K. Shi, B.Y. Chu, M.Y. Lei, K.K. Huang, Y.C. Gu, Z.Y. Qian, Biomineralized polymer matrix composites for bone tissue repair:a review, Sci. China Chem. 61 (2018) 1553–1567.
[50] J.H. Du, Y. Zhou, X.G. Bao, Z.R. Kang, J.M. Huang, G.H. Xu, C.Q. Yi, D.J. Li, Surface polydopamine modification of bone defect repair materials: characteristics and applications, Front. Bioeng. Biotechnol. 10 (2022), 974533.
[51] B. Li, R. Huang, J. Ye, L. Liu, L. Qin, J.H. Zhou, Y.F. Zheng, S.L. Wu, Y. Han, A self- healing coating containing curcumin for osteoimmunomodulation to ameliorate osseointegration, Chem. Eng. J. 403 (2021), 126323.
[52] T. Sun, D. Hu, Z.Z. Guo, H.W. Gong, Q.W. Xin, Y.D. Mu, J. Weng, J.S. Li, X. Y. Chen, Hexapeptide decorated beta-cyclodextrin delivery system for targeted therapy of bone infection, J. Contr. Release 353 (2023) 337–349.
[53] K. Papadimitriou, G. Karkavelas, I. Vouros, E. Kessopoulou, A. Konstantinidis, Effects of local application of simvastatin on bone regeneration in femoral bone defects in rabbit, J. Cranio. Maxill. Surg. 43 (2015) 232–237.
[54] M. Kuwahara, Y. Akasaki, N. Goto, I. Kurakazu, T. Sueishi, M. Toya, T. Uchida, T. Tsutsui, R. Hirose, H. Tsushima, Y. Nakashima, Fluvastatin promotes chondrogenic differentiation of adipose-derived mesenchymal stem cells by inducing bone morphogenetic protein 2, BMC Pharmacol. Toxicol. 23 (2022) 61.
[55] Y. Misuzu, O. Fumio, M. Tomoyuki, O. Hiroyuki, I. Kenichi, M. Tomoko, G. Junko, Y. Masahiro, M. Hirofumi, Simvastatin antagonizes tumor necrosis factor-α inhibition of bone morphogenetic proteins-2-induced osteoblast differentiation by regulating Smad signaling and Ras/Rho-mitogen-activated protein kinase pathway, Mol. Cell. Endocrinol. 350 (2012) 78–86.
[56] S.N. Raafat, R.M. Amin, M.M. Elmazar, M.M. Khattab, A.S. El-Khatib, The sole and combined effect of simvastatin and platelet rich fibrin as a filling material in induced bone defect in tibia of albino rats, Bone 117 (2018) 60–69.
[57] S.C. Wu, C.H. Chang, L.H. Chang, C.W. Wu, J.W. Chen, C.H. Chen, Y.S. Lin, J. K. Chang, M.L. Ho, Simvastatin enhances the chondrogenesis but not the osteogenesis of adipose-derived stem cells in a hyaluronan microenvironment, Biomedicines 9 (2021) 559.
[58] H.A. Rather, R. Patel, U. Yadav, R. Vasita, Dual drug-delivering polycaprolactone-collagen scaffold to induce early osteogenic differentiation and coupled angiogenesis, Biomed. Mater. 15 (2020), 045008.
[59] S.Y. Zhao, S.B. Yu, D.G. Zhu, L. Dai, P.P. Yang, X.H. Xing, Stimulatory effects of simvastatin on bone regeneration of the expanded suture in rats, Am. J. Transl. Res. 12 (2020) 1767–1778.
[60] J.K. Liao, U. Laufs, PLEIOTROPIC effects of STATINS-annual review of pharmacology and toxicology, Annu. Rev. Pharmacol. Toxicol. 45 (2005) 89.
[61] X.W. Wang, K.Y. Yan, C.F. Wen, J.Q. Wang, Simvastatin combined with resistance training improves outcomes in patients with chronic heart failure by modulating mitochondrial membrane potential and the janus kinase/signal transducer and activator of transcription 3 signaling pathways, Cardiovasc. Ther. 2022 (2022), 8430733.
[62] D. Zhang, Z.H. Gu, J.X. Wang, Y. Zhang, Y. Zheng, Apocynum leaf extract suppresses the progress of atherosclerosis in rats via the FKN/SYK/p38 signal pathway, Evid. Based. Compl. Alt. Med. 2021 (2021), 5524226.
[63] H.P. Liu, J.F. Li, X.M. Liu, Z.Y. Li, Y. Zhang, Y.Q. Liang, Y.F. Zheng, S.L. Zhu, Z. D. Cui, S.L. Wu, Photo-sono interfacial engineering exciting the intrinsic property of herbal nanomedicine for rapid broad-spectrum bacteria killing, ACS Nano 15 (2021) 18505–18519.
[64] Z.Y. Zhang, Y.L. An, X.S. Wang, L.Y. Cui, S.Q. Li, C.B. Liu, Y.H. Zou, F. Zhang, R. C. Zeng, In vitro degradation, photo-dynamic and thermal antibacterial activities of Cu-bearing chlorophyllin-induced Ca-P coating on magnesium alloy AZ31, Bioact. Mater. 18 (2022) 284–299.

[65] J. Gao, L. Hao, R.J. Jiang, Z. Liu, L.M. Tian, J. Zhao, W.H. Ming, L. Ren, Surprisingly fast assembly of the MOF film for synergetic antibacterial phototherapeutics, Green Chem. 24 (2022) 5930–5940.
[66] K.N. Zhu, S.Y. Qian, H.W. Guo, Q.Y. Wang, X.Y. Chu, X.Y. Wang, S. Lu, Y. Peng, Y. S. Guo, Z.Q. Zhu, T.Y. Qin, B. Liu, Y.W. Yang, B.L. Wang, pH-activatable organic nanoparticles for efficient low-temperature photothermal therapy of ocular bacterial infection, ACS Nano 16 (2022) 11136–11151.
[67] M. Hockel, P. Vaupel, Tumor hypoxia: definitions and current clinical, biologic, and molecular aspects, J. Natl. Cancer Inst. 93 (2001) 266–276.
[68] L. Tan, J. Li, X.M. Liu, Z.D. Cui, X.J. Yang, S.L. Zhu, Z.Y. Li, X.B. Yuan, Y.F. Zheng, K.W.K. Yueung, H.B. Pan, X.B. Pan, X.B. Wang, S.L. Wu, Rapid biofilm eradication on bone implants using red phosphorus and near-infrared light, Adv. Mater. 30 (2018) 1801–1808.
[69] F. Perreault, A.D. Faria, S. Nejati, M. Elimelech, Antimicrobial properties of graphene oxide nanosheets: why size matters, ACS Nano 9 (2015) 7226–7236.
[70] Q. Zhang, M.Y. Wu, Y.Y. Fang, C. Deng, H.H. Shen, Y. Tang, Y.J. Wang, Dendritic mesoporous silica hollow spheres for nano-bioreactor application, Nanomaterials 12 (2022) 1940.
[71] X.P. Wang, X. Li, A. Ito, Y. Sogo, T. Ohno, Synergistic anti-tumor efficacy of a hollow mesoporous silica-based cancer vaccine and an immune checkpoint inhibitor at the local site, Acta Biomater. 145 (2022) 235–245.
[72] L.D. Hu, J.Y. Ma, X.J. Wei, Y.Z. Li, S.H. Jiang, X.X. Ji, F.K. Zhu, H.X. Tan, P. Y. Wang, Biodegradable polydopamine and tetrasulfide bond co-doped hollowed mesoporous silica nanospheres as GSH-triggered nanosystem for synergistic chemo-photothermal therapy of breast cancer, Mater. Des. 215 (2022), 110467.
[73] L. Abdollahi, M.J. Dianat, M.D. Marcos, R. Martinez-Manez, S. Karimi, Hollow mesoporous silica nanoparticles: effective silica etching using tri-di- and mono-valent cations, Biomater. Adv. 133 (2022), 112621.
[74] D.L. Han, Y. Li, X.M. Liu, K.W.K. Yeung, Y.F. Zheng, Z.D. Cui, Y.Q. Liang, Z.Y. Li, S.L. Zhu, X.B. Wang, S.L. Wu, Photothermy-strengthened photocatalytic activity of polydopamine-modified metal-organic frameworks for rapid therapy of bacteria-infected wounds, J. Mater. Sci. Technol. 62 (2022) 83–95.
[75] Y.M. Zhou, C. Chang, Z.H. Liu, Q.L. Zhao, N.Q. Xu, C.H. Li, Y.Q. Chen, Y.L. Zhang, B. Lu, Hyaluronic acid-functionalized hollow mesoporous silica nanoparticles as pH- sensitive nanocarriers for cancer chemo-photodynamic therapy, Langmuir 37 (2021) 2619–2628.
[76] Y.P. Shi, M.Y. Zhou, Y. Zhang, Y.F. Wang, J.L. Cheng, MRI-guided dual-responsive anti- tumor nanostructures for synergistic chemo-photothermal therapy and chemodynamic therapy, Acta Biomater. 158 (2023) 571–582.
[77] M. Pfau, F. Beltran, L. Woodard, L. Dobson, S. Gasson, A. Robbins, Z. Lawson, W. B. Saunders, M. Moreno, M. Grunlan, Evaluation of a self-fitting, shape memory polymer scaffold in a rabbit calvarial defect model, Acta Biomater. 136 (2021) 233–242.
[78] D.W. Zhang, O.J. George, K.M. Petersen, A.C. Jimenez-Vergara, M.S. Hahn, M. A. Grunlan, A bioactive "self-fitting" shape memory polymer scaffold with potential to treat cranio-maxillo facial bone defects, Acta Biomater. 10 (2014) 4597–4605.
[79] J.M.S. Shah, B. Lundquist, J. Macaitis, M.R.P. Cloud, F.O. Beltran, M.A. Grunlan, W. Lien, H.C. Wang, A.J. Burdette, Comparative evaluation of mesenchymal stromal cell growth and osteogenic differentiation on a shape memory polymer scaffold, J. Biomed. Mater. Res. 110 (2022) 2063–2074.
[80] F.O. Beltran, C.J. Houk, M.A. Grunlan, Bioactive siloxane-containing shape-memory polymer (SMP) scaffolds with tunable degradation rates, ACS Biomater. Sci. Eng. 7 (2021) 1631–1639.
[81] A. Gupta, C. Srivastava, Electrodeposition current density induced texture and grain boundary engineering in Sn coatings for enhanced corrosion resistance, Corros. Sci. 194 (2022), 109945.
[82] S.Q. Yin, W.C. Duan, W.H. Liu, L. Wu, J.M. Yu, Z.L. Zhao, M. Liu, P. Wang, J. Z. Cui, Z.Q. Zhang, Influence of specific second phases on corrosion behaviors of Mg-Zn-Gd-Zr alloys, Corros. Sci. 166 (2019), 108419.
[83] L.Y. Cui, S.D. Gao, P.P. Li, R.C. Zeng, F. Zhang, S.Q. Li, E.H. Han, Corrosion resistance of a self-healing micro-arc oxidation/polymethyltrimethoxysilane composite coating on magnesium alloy AZ31, Corros. Sci. 118 (2017) 84–95.
[84] Y.B. Zhao, H.P. Liu, C.Y. Li, Y. Chen, S.Q. Li, R.C. Zeng, Z.L. Wang, Corrosion resistance and adhesion strength of a spin-assisted layer-by-layer assembled coating on AZ31 magnesium alloy, Appl. Surf. Sci. 434 (2018) 787–795.
[85] A.I. Rezk, H.M. Mousa, J. Lee, C.H. Park, C.S. Kim, Composite PCL/HA/simvastatin electrospun nanofiber coating on biodegradable Mg alloy for orthopedic implant application, J. Coating Technol. Res. 16 (2018) 477–489.
[86] B. Rabadiya, DRUG-EXCIPIENTS interaction and solubility enhancement study of simvastatin, Int. J. Pharm. Res. Bio. Sci. 2 (2013) 168–185.
[87] L.G. Wang, S.K. Guan, X. Ma, S.J. Zhu, H.X. Wang, Formation mechanism of Ca-deficient hydroxyapatite coating on Mg-Zn-Ca alloy for orthopaedic implant, Appl. Surf. Sci. 307 (2014) 92–100.
[88] H.X. Wang, S.K. Guan, X. Wang, C.X. Ren, L.G. Wang, In vitro degradation and mechanical integrity of Mg-Zn-Ca alloy coated with Ca-deficient hydroxyapatite by the pulse electrodeposition process, Acta Biomater. 6 (2010) 1743–1748.
[89] K. Xue, P.H. Tan, Z.H. Zhao, L.Y. Cui, M.B. Kannan, S.Q. Li, C.B. Liu, Y.H. Zou, F. Zhang, Z.Y. Chen, R.C. Zeng, In vitro degradation and multi-antibacterial mechanisms of beat-cyclodextrin@curcumin embodied Mg(OH)2/MAO coating on AZ31 magnesium alloy, J. Mater. Sci. Technol. 132 (2023) 179–192.
[90] Y.B. Zhao, Z. Zhang, L.Q. Shi, F. Zhang, S.Q. Li, R.C. Zeng, Corrosion resistance of a self-healing multilayer film based on SiO2 and CeO2 nanoparticles layer-by-layer assembly on Mg alloys, Mater. Lett. 37 (2019) 14–18.
[91] W. Xu, L. Feng, X.W. Zheng, J.Q. Sun, Water-enabled self-healing of polyelectrolyte multilayer coatings, Angew. Chem. Int. Ed. 50 (2011) 11378–11381.
[92] Y. Li, S.S. Chen, M.C. Wu, J.Q. Sun, Polyelectrolyte multilayers impart healability to highly electrically conductive films, Adv. Mater. 24 (2012) 4578–4582.
[93] Y. Zhang, S.E. Chen, J.L. Shao, J.J.P. van den Beucken, Combinatorial surface roughness effects on osteoclastogenesis and osteogenesis, ACS Appl. Mater. Interfaces 10 (2018) 36652–36663.
[94] P.C. Wong, S.M. Song, P.H. Tsai, Y.Y. Nien, J.S. Jang, C.K. Cheng, C.H. Chen, Relationship between the surface roughness of biodegradable Mg-based bulk metallic glass and the osteogenetic ability of MG63 osteoblast-like cells, Materials 13 (2020) 1188.
[95] Y.P. Liu, Y.X. Wang, X. Cheng, Y. Zheng, M.Y. Lyu, P. Di, Y. Lin, MiR-181d-5p regulates implant surface roughness-induced osteogenic differentiation of bone marrow stem cells, Mater. Sci. Eng. C 121 (2021), 111801.
[96] X.J. Zan, P. Sitasuwan, S. Feng, Q. Wang, Effect of roughness on in situ biomineralized CaP-collagen coating on the osteogenesis of mesenchymal stem cells, Langmuir 32 (2016) 1808–1817.
[97] Z. Geng, R.F. Wang, X.L. Zhuo, Z.Y. Li, Y.C. Huang, L.L. Ma, Z.D. Cui, S.L. Zhu, Y. Q. Liang, Y.D. Liu, H.J. Bao, X. Li, Q.Y. Huo, Z.L. Liu, X.J. Yang, Incorporation of silver and strontium in hydroxyapatite coating on titanium surface for enhanced antibacterial and biological properties, Mater. Sci. Eng. C 71 (2017) 852–861.
[98] J. Munoz, N.S. Akhavan, A.P. Mullins, B.H. Arjmandi, Macrophage polarization and osteoporosis: a review, Nutrients 12 (2020) 2999.
[99] X.S. Tong, G.S. Yu, X.H. Fu, R.L. Song, J.H. Gu, Z.P. Liu, A review of signaling transduction mechanisms in osteoclastogenesis regulation by autophagy, inflammation, and immunity, Int. J. Mol. Sci. 23 (2022) 9846.
[100] P.C. Zhou, T. Zheng, B.H. Zhao, Cytokine-mediated immunomodulation of osteoclastogenesis, Bone 164 (2022), 116540.
[101] R.A. Kumar, Y. Li, Q.J. Dang, F. Yang, Monocytes in rheumatoid arthritis: circulating precursors of macrophages and osteoclasts and, their heterogeneity and plasticity role in RA pathogenesis, Int. Immunopharm. 65 (2018) 348–359.
[102] B. Thapa, K. Lee, Metabolic influence on macrophage polarization and pathogenesis, BMB Rep. 52 (2019) 360–372.
[103] W. Zhang, C.G. Sun, J.X. Zhu, W.F. Zhang, H.J. Leng, C.L. Song, 3D printed porous titanium cages filled with simvastatin hydrogel promotes bone ingrowth and spinal fusion in rhesus macaques, Biomater. Sci. 8 (2020) 4147–4156.
[104] H.F. Qi, K. Wang, M. Li, Y.N. Zhang, K. Dong, S. Heise, A.R. Boccaccini, T.L. Lu, Co-culture of BMSCs and HUVECs with simvastatin-loaded gelatin nanosphere/chitosan coating on Mg alloy for osteogenic differentiation and vasculogenesis, Int. J. Biol. Macromol. 193 (2021) 2021–2028.
[105] Y.X. Sun, X.D. Liu, X.L. Zeng, L.P. Wang, Z. Jin, K.W.K. Yeung, X.Y. Liu, L. P. Ouyang, Y. Liao, Simvastatin-loaded sulfonated PEEK enhances angiogenesis and osteogenesis via miR-29cb2-mediated HIF-3α downregulation, Chem. Eng. J. 448 (2022), 137738.
[106] H. Jin, Y.B. Ji, Y.T. Cui, L. Xu, H. Liu, J.C. Wang, Simvastatin-incorporated drug delivery systems for bone regeneration, ACS Biomater. Sci. Eng. 7 (2021) 2177–2191.
[107] B.Y. Dai, X. Li, J.K. Xu, Y.W. Zhu, L. Huang, W.X. Tong, H. Yao, D.H. Chow, L. Qin, Synergistic effects of magnesium ions and simvastatin on attenuation of high-fat diet-induced bone loss, Bioact. Mater. 6 (2021) 2511–2522.